


Geometry of Almost-Conserved Quantities in Symplectic Maps

Part I. Perturbation Theory

T. Zolkin *

Independent Researcher, Chicago, IL

S. Nagaitsev 

*Brookhaven National Laboratory, Upton, NY 11973 and
Old Dominion University, Norfolk, VA 23529*

I. Morozov 

*Synchrotron Radiation Facility “SKIF”, Koltsovo 630559, Russia and
Novosibirsk State Technical University, Novosibirsk 630073, Russia*

S. Kladov 

University of Chicago, Chicago, IL 60637

(Dated: June 12, 2025)

Noether’s theorem, which connects continuous symmetries to exact conservation laws, remains one of the most fundamental principles in physics and dynamical systems. In this work, we draw a conceptual parallel between two paradigms: the emergence of exact invariants from continuous symmetries, and the appearance of approximate invariants from discrete symmetries associated with reversibility in symplectic maps. We demonstrate that by constructing approximating functions that preserve these discrete symmetries order by order, one can systematically uncover hidden structures, closely echoing Noether’s framework. The resulting functions serve not only as diagnostic tools but also as compact representations of near-integrable behavior.

The first article establishes the formal foundations of the method. Using the symmetric form of the map as a flexible test case, we benchmark the perturbative construction against established techniques, including the Lie algebra method for twist coefficients. To resolve the inherent ambiguity in the perturbation series, we introduce an averaging procedure that naturally leads to a resonant theory — capable of treating rational rotation numbers and small-denominator divergences. This enables an accurate and structured description of low-order resonances, including singular and non-singular features in the quadratic and cubic Hénon maps. The approach is systematic, requiring only linear algebra and integrals of elementary functions, yet it yields results in striking agreement with both theory and numerical experiment. We conclude by outlining extensions to more general maps and discussing implications for stability estimates in practical systems such as particle accelerators.

I. INTRODUCTION

Among the most profound results in dynamical systems theory, few have influenced our understanding of long-term behavior as deeply as the KAM theory [1–3], Nekhoroshev stability estimates [4], and Aubry-Mather theory [5]. These cornerstone developments reveal how order and structure can persist within nonlinear Hamiltonian systems, even under perturbation — bridging the divide between integrability and chaos. Together, they establish a robust framework for understanding stability, quasi-periodicity, and the delicate onset of transport and diffusion in complex systems [6].

Equally foundational is Noether’s theorem [7], which forged the deep and elegant connection between symmetry and conservation. In essence, it states that every continuous symmetry of the action yields a conserved quantity, a principle that underlies classical mechanics, field theory, and quantum physics alike [8, 9]. Time

translation implies energy conservation; spatial translation gives linear momentum; rotational symmetry yields angular momentum. But more than just a practical tool, Noether’s theorem offers a structural lens — one that organizes and simplifies complex systems through their symmetries.

Despite the formal complexity of these theorems, their implications resonate even in practical settings. From planetary stability [10–12] to modern accelerators [13, 14], we see that nonlinear systems often exhibit a surprising robustness: long-term ordered motion, persistence of invariant structures, and even the survival of near-integrals in strongly perturbed regimes.

This report turns to a related but distinct setting: discrete-time, symplectic, and reversible dynamical systems/mappings — a class dating back to G.D. Birkhoff [15] and explored in depth by R.J. De Vogelaere [16], D.C. Lewis [17] and rigorously outlined in a report by J.A.G. Roberts and G.R.W. Quispel [18]. A system is *reversible* if there exists an involution in phase space — an operation that undoes itself — that reverses the direction of time. For maps, this means they can be decomposed into the product of two such involutions.

* iguanodyn@gmail.com

This structure implies a rich algebra of symmetries: even chaotic reversible maps possess an infinite discrete symmetry group generated by compositions of involutions and map iterates.

Here, we ask: can these symmetries help uncover approximate invariants in chaotic or near-integrable systems — especially in settings where traditional integrals are no longer exact? For an integrable map of the plane M , the invariant function satisfies

$$\mathcal{K}[M(p, q)] - \mathcal{K}[p, q] = 0$$

for any values of $(p, q) \in \mathbb{R}^2$, and is itself invariant not only under the map, but both involutions comprising it. This property, famously utilized by McMillan in constructing an integrable map, extends beyond integrable cases: even in chaotic systems, invariant structures tend to reflect the underlying symmetries of the map. These symmetries aid in identifying symmetric fixed points, n -cycles, and organizing bifurcations, see, for example, [18, 19].

Building on this insight, we propose a perturbative framework that generalizes this idea. Rather than demanding exact invariance, we construct an approximate invariant

$$\mathcal{K}^{(n)}[T(p, q)] - \mathcal{K}^{(n)}[p, q] = \mathcal{O}(\epsilon^{n+1})$$

where T is a general symplectic, possibly chaotic map. This deceptively simple condition — requiring that the function is preserved up to a given order — proves to be a powerful principle. It allows us to: (i) match twist coefficients (expansion of rotation number on action variable), consistent with Lie algebra techniques; (ii) recover normal forms for low-order nonlinear resonances, that perfectly align with numerical experiments; (iii) reconstruct global invariant curves for exactly integrable systems; and (iv) approximate the geometry of island chains and low-order KAM structures. The method itself is systematic and relies only on solving linear systems and, when necessary, integrating powers of trigonometric functions to handle small denominator problems. This makes it not only analytically tractable, but also geometrically illuminating.

A particularly striking outcome is that approximate invariants derived in this way naturally inherit the discrete symmetries of the system — mirroring the role continuous symmetries play in Noether’s theorem. Symmetry, once again, becomes the organizing principle behind conservation — even if only approximately.

As a benchmark, we provide a next-order extension of the Courant-Snyder [20] invariant used in accelerator physics, incorporating leading nonlinear terms. Numerous examples are explored, including real-world applications.

We believe that this approach — simple in its construction yet rich in implications — offers a promising tool for probing structures in nonlinear maps and opens the door to deeper insights into the resilience of order in chaotic systems.

A. Motivation and preliminary remarks

In the study of dynamical systems — particularly within symplectic and Hamiltonian mechanics — Lie algebras and Lie transformations serve as powerful tools for computing *action-angle variables* and *twist coefficients* τ_i , which characterize how the angle variable θ evolves with the action J , i.e., how the nonlinear *frequency* ν shifts with amplitude. The central idea is to transform the Hamiltonian (or map) into a canonical form [21–24]:

$$\mathcal{H}[J, \theta; t] = \nu_0 J + \frac{\tau_0}{2!} J^2 + \frac{\tau_1}{3!} J^3 + \dots,$$

in which the Hamiltonian depends solely on the action J , achieved through a sequence of Lie transformations. This formalism systematically eliminates angle dependence order by order.

In accelerator physics, Lie algebra methods have been successfully employed to optimize lattice designs by removing *singular* resonances [25–27] — those for which the detuning $d\nu/dJ$ diverges at $J = 0$. Additionally, determining the shift in frequency (or *rotation number/betatron tune* in the discrete-time case) as a function of amplitude is crucial for estimating thresholds of collective instabilities and Landau damping [28, 29] required for their mitigation [30, 31].

These transformations effectively straighten the motion: in the transformed coordinates, trajectories trace circles, the action remains invariant, and the angle increases linearly in time, governed by an amplitude-dependent frequency. However, this elegant behavior holds only in regions of regular, bounded motion — and this is where the complications begin.

Typically, integrable systems possess *separatrices* — boundaries dividing regions of qualitatively different motion. These are formed by stable and unstable manifolds of hyperbolic (unstable) fixed points and/or periodic orbits (n -cycles). As a result, any action-angle formulation is inherently local, valid only within regions enclosed by separatrices, and fails to describe the global phase space structure. The issue is even more severe in chaotic systems, where the very concept of a simply connected domain of stability may break down. In such systems, even an infinitesimally small amplitude motion may be interrupted by chains of islands, arising from the breakdown of invariant tori [32].

This motivates the development of perturbative methods that can complement the Lie algebra approach. Unlike Lie techniques, which focus on infinitesimal neighborhoods around stable fixed points, perturbative methods aim to provide meaningful estimates beyond the separatrix, potentially navigating through island chains and capturing aspects of the broader dynamics.

To illustrate these ideas and set the stage for further discussion, we begin with the case of continuous-time dynamics. Although our eventual perturbative construction will differ in specifics, this preliminary discussion highlights the challenges and outlines alternative strategies.

As examples, consider the three following classical Hamiltonians:

$$\begin{aligned}\mathcal{H}_1[p, q; t] &= \frac{p^2}{2} + \frac{q^2}{2} - \frac{q^4}{4}, \\ \mathcal{H}_2[p, q; t] &= \frac{p^2}{2} + \frac{q^2}{2} - \frac{3}{2\sqrt{2}} \frac{q^3}{3} + \frac{1}{4} \frac{q^4}{4}, \\ \mathcal{H}_3[p, q; t] &= \frac{p^2}{2} + \frac{q^2}{2} + \sum_{i=0}^{\infty} \frac{\tau_i}{(i+2)!} \left(\frac{p^2 + q^2}{2} \right)^{i+2},\end{aligned}$$

each representing different nonlinear oscillators.

The first system is a classical harmonic oscillator with a cubic nonlinearity, i.e., it includes a restoring force of the form $F(q) = -q + q^3$. The second system, though perhaps less familiar in this form, can be derived from the Duffing oscillator [33]:

$$H_{\text{Duff.}}[p, Q; t] = \frac{p^2}{2} - \frac{Q^2}{2} + \frac{Q^4}{4},$$

by rescaling time via $t = t/\sqrt{2}$, with the corresponding shift of the origin according to $Q = (q-1)/\sqrt{2}$ and $H_{\text{Duff.}} = \mathcal{H}_2 - \frac{1}{4}$.

The third system is defined for

$$J \leq J_{\text{max}} = \frac{2^{3/2}}{3\pi}$$

where J is the canonical action variable, proportional to the area enclosed by an invariant torus in phase space (i.e., a level set of constant $\mathcal{H}_3[p, q] = \text{const}$):

$$J = \frac{1}{2\pi} \oint p dq = \frac{p^2 + q^2}{2}.$$

Accordingly, the Hamiltonian is naturally expressed in terms of action-angle variables and takes the form

$$\mathcal{H}_3[J, \theta; t] = \nu_0 J + \sum_{i=0}^{\infty} \frac{\tau_i}{(i+2)!} J^{i+2}, \quad \nu_0 = 1.$$

It is independent of the angle variable θ , reflecting an exact continuous symmetry and, by Noether's Theorem, guaranteeing conservation of the action J .

The twist coefficients τ_i describe the frequency's dependence on the action via a power series:

$$\nu = \frac{d\theta}{dt} = \frac{\partial \mathcal{H}}{\partial J} = \nu_0 + \sum_{i=0}^{\infty} \frac{\tau_i}{(i+1)!} J^{i+1}$$

and for this example we choose them to match the series

$$\nu(J) = 1 - \frac{3}{4} J - \frac{51}{64} J^2 - \frac{375}{256} J^3 - \frac{53445}{16384} J^4 + \mathcal{O}(J^5)$$

which arises from an implicit dependence given by:

$$\begin{aligned}\nu(\kappa) &= \frac{\pi}{2} \frac{K^{-1}[\kappa]}{\sqrt{1+\kappa^2}}, \\ J(\kappa) &= \frac{4}{3\pi} \frac{1}{\sqrt{1+\kappa^2}} \left(E[\kappa] - \frac{1-\kappa^2}{1+\kappa^2} K[\kappa] \right),\end{aligned}\tag{1}$$

where $K[\kappa]$ and $E[\kappa]$ are the *complete elliptic integrals of the first and second kind*, respectively, and $\kappa \in [0, 1]$ is the *elliptic modulus*.

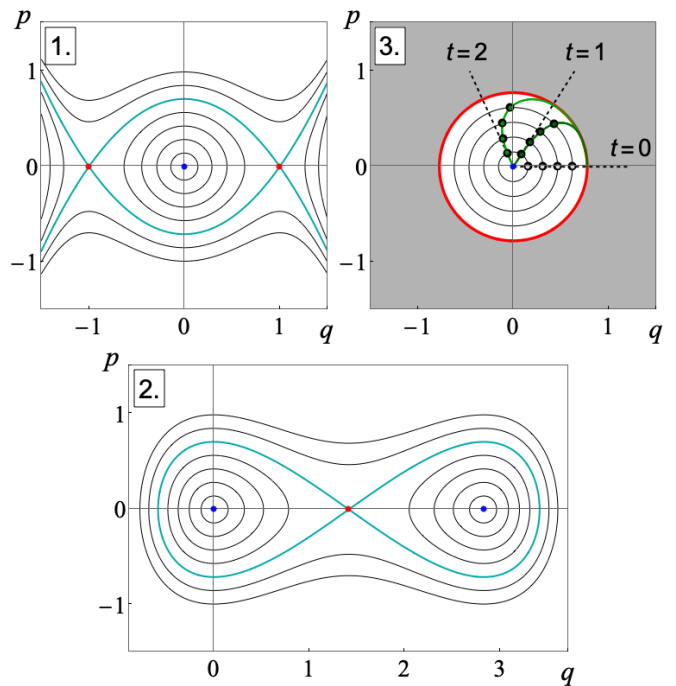


FIG. 1. Constant level sets of Hamiltonians $\mathcal{H}_{1,2,3}[p, q]$. Blue and red points mark stable (*elliptic centers*) and unstable (*hyperbolic saddles*) stationary solutions, respectively. Cyan curves indicate (homo-)heteroclinic connections forming separatrices between different types of motion. In the third plot, the gray region denotes the domain where the Hamiltonian is not defined. Additionally, the last plot illustrates a sequence of points selected on invariant curves and along the line $q = 0$ at $t = 0$, along with their images under the dynamics at $t = 1$ and $t = 2$. Green lines show the forward iterates of an entire segment of the $p > 0$ half-line.

Interestingly enough, while we did some “magic” by purposefully matching action angle variables of Hamiltonians \mathcal{H}_1 to \mathcal{H}_3 by construction, the Hamiltonian \mathcal{H}_2 also has exactly the same $\nu(J)$ dependence around the stationary point at the origin, given by Eqs. (1). Plots 1 through 3 in Fig. 1 provide phase space diagrams with level sets of corresponding Hamiltonians, and we see that despite exactly the same description of dynamics within the simply connected region, the complete picture differs a lot. At large amplitudes, in case (1.) we have unstable motion, in case (2.) stable orbits rounding the origin, and in case (3.) the system is not defined. Moreover, even at the boundary of motions, in the first case we have a separatrix made of a *heteroclinic connection* between two different saddles, two *homoclinic orbits* attached to a single unstable solution in case (2.), and a boundary completely made of fixed points in the last case. This example illustrates how information is inevitably lost beyond $J \geq J_{\text{max}}$, even if all twist coefficients τ_i are known and/or a closed-form expression for $\nu(J)$ is available. The left plot in Fig. 2 shows the dependence of $\nu(J)$, compared to its truncated power series approximations.

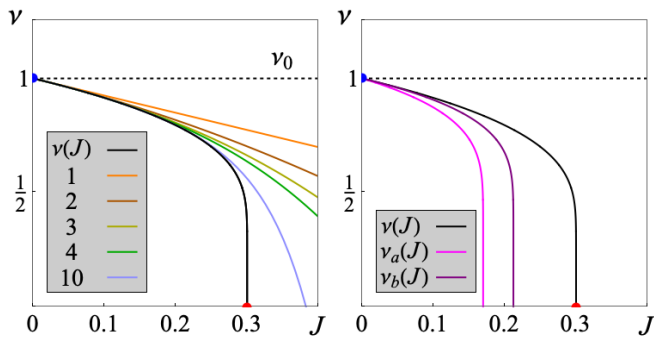


FIG. 2. Frequency of oscillations $\nu(J)$ as a function of the action variable for the model Hamiltonians $\mathcal{H}_{1,2,3}$ (black curve). The left plot shows power series approximations of the form $\nu_n(J) \approx \nu_0 + \tau_0 J + \dots + \tau_{n-1} J^n$, while the right plot compares these with approximations obtained from Hamiltonians featuring cubic potentials.

With that in mind, while the transformation to action-angle variables effectively “blinds” us beyond the separatrix, the original Hamiltonian equations of motion,

$$\frac{dq}{dt} = \frac{\partial \mathcal{H}}{\partial p} \quad \text{and} \quad \frac{dp}{dt} = -\frac{\partial \mathcal{H}}{\partial q},$$

still contain full information about the system, including the globally conserved values of \mathcal{H} .

Now, focusing on case 2, suppose we do not know the exact invariant $\mathcal{H}_2[p, q]$, but we do have access to the equations of motion. Further, imagine we’ve developed a perturbative approach capable of reconstructing the invariant from the equations of motion in the form of a polynomial. Then, in zeroth order (often referred to as a *linearization*), we would recover the harmonic oscillator:

$$\mathcal{H}_0[p, q; t] = \frac{p^2}{2} + \frac{q^2}{2}.$$

While this oversimplified approximation cannot predict any nonlinear phenomena — such as detuning or even the presence (let alone the location) of a separatrix — it still provides the correct *bare* frequency $\nu_0 = \nu(0)$.

In the next order, we can imagine that our hypothetical perturbation theory successfully recovers the cubic term in the potential energy (corresponding to the quadratic term in the restoring force):

$$\mathcal{H}_{2.a}[p, q; t] = \frac{p^2}{2} + \frac{q^2}{2} - \frac{3}{2\sqrt{2}} \frac{q^3}{3}.$$

The right plot in Fig. 2 illustrates the corresponding frequency-action dependence $\nu_a(J)$. What is immediately apparent is that although the prediction for the location of the separatrix is underestimated by almost a factor of two, the behavior of $\nu_a(J)$ captures the qualitative aspect far better than the traditional power series shown in the left plot. However, one key issue remains: the approximate Hamiltonian $\mathcal{H}_{2.a}[p, q; t]$ fails to reproduce the correct twist coefficient $\tau_0 = -3/4$, yielding instead an incorrect value of $-15/16$.

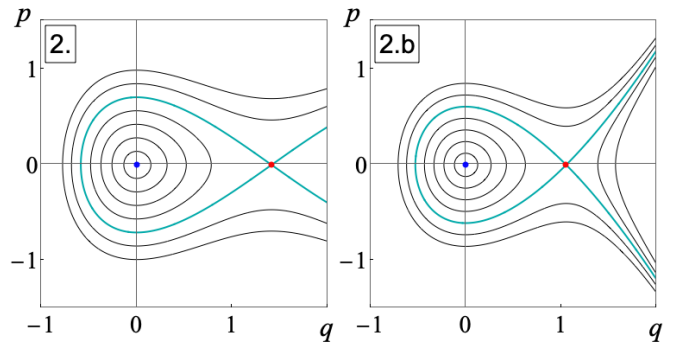


FIG. 3. Constant level sets of Hamiltonians \mathcal{H}_2 and $\mathcal{H}_{2.b}$.

Thus, before proceeding to recover the next order term, we can attempt to refine our approximation within the same order by modifying it:

$$\mathcal{H}_{2.b}[p, q; t] = \frac{p^2}{2} + \frac{q^2}{2} - \frac{3}{\sqrt{10}} \frac{q^3}{3}$$

so that it restores the correct value of $\tau_0 = -3/4$. Looking at the behavior of the refined frequency $\nu_{2.b}(J)$ shown in Fig. 2, we see that although it still deviates, the estimated location of the separatrix now achieves accuracy comparable in absolute value with the tenth order of the traditional power series — and once again provides much better qualitative agreement. Additionally, Fig. 3 presents a direct comparison of the level sets defined by the exact Hamiltonian \mathcal{H}_2 and its approximation $\mathcal{H}_{2.b}$. While the approximation still cannot describe the dynamics beyond the separatrix, it captures its presence and essential qualitative features of the motion within its vicinity remarkably well.

We now shift focus to the central subject of this article: *symplectic mappings* of the plane [34], defined by a pair of coupled equations

$$\begin{aligned} q' &= f_1(q, p), \\ p' &= f_2(q, p), \end{aligned}$$

where we will use the prime symbol ($'$) throughout to denote the image under one application of the map. Symplectic maps preserve phase space volume and the underlying geometric structure, mapping infinitesimal elements to others of equal measure. For maps of the plane, this symplectic condition is equivalent to the conservation of phase space area.

One way such maps arise is through discretizing the continuous-time flow of a Hamiltonian system with one degree of freedom at equidistant time intervals. These mappings are necessarily integrable, possessing an exact integral of motion (given by any function of the generating Hamiltonian itself). An example of such a discretization, applied to the Hamiltonian \mathcal{H}_3 is shown in plot (3.) of Fig. 1. The resulting map serves as an example of a nonlinear, integrable *twist map* [2, 34].

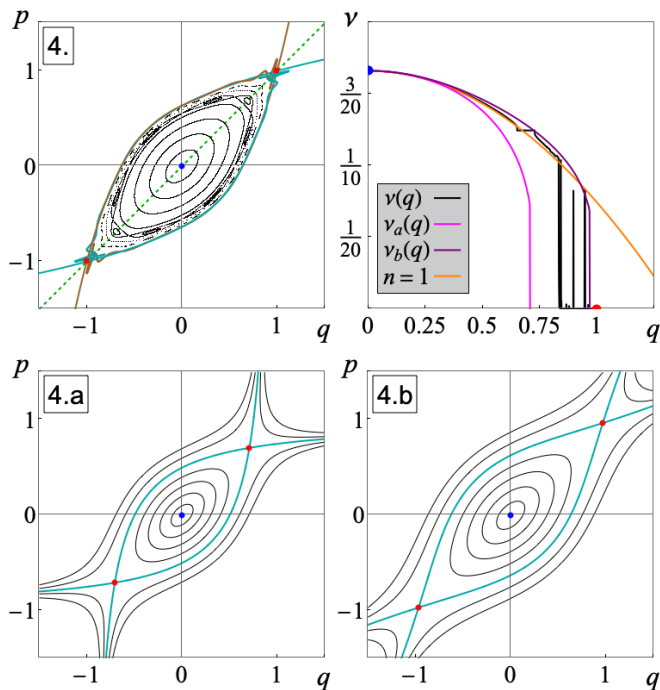


FIG. 4. Top left: Some invariant structures of the cubic Hénon map with $f(p) = p + p^3$, including surviving KAM circles (black), a stable fixed point (blue), unstable fixed points (red), and their associated stable and unstable manifolds (brown and cyan), computed via continuation of linearized eigenvectors. The dashed green line indicates the first symmetry, $p = q$. Top right: Rotation number $\nu(q)$ along the symmetry line (black curve), alongside several approximations: the quadratic truncation of the traditional power series $\nu(q) = \nu_0 + (2\pi\sqrt{3})^{-1}q^2$, the integrable McMillan-based approximation $\nu_{4,a}(q)$, and a refined version derived from the averaged invariant of the same order $\nu_{4,b}(q)$. Bottom: Level sets of the approximated invariants $\mathcal{K}_{4,a}[p, q]$ and $\mathcal{K}_{4,b}[p, q]$.

Another route to symplectic maps involves taking a *stroboscopic Poincaré section* at times $t_k = kT$ of a non-autonomous Hamiltonian system with one degree of freedom that is subject to a time-periodic external force (with period T). Alternatively, they can arise from regular Poincaré sections of autonomous Hamiltonians with two degrees of freedom [32]. Famous examples include the chaotic Chirikov standard map [35, 36] and the Hénon–Heiles potential [37]. In contrast to the previous (integrable) case, these systems generally exhibit chaos, with integrability being the exception rather than the rule [38–42].

Before diving into the construction and analysis of our perturbative method, let’s preview what’s to come through one more illustrative example, the chaotic Hénon map [19, 43–46] with a cubic force $f(p) = p + p^3$:

$$\begin{aligned} q' &= p, \\ p' &= -q + f(p). \end{aligned}$$

Much like the previously discussed Hamiltonian

$\mathcal{H}_1[p, q; t]$, this map possesses a stable fixed point at the origin, as well as two unstable fixed points — this time located along the first symmetry line $p = q$. However, in this case, the stable and unstable manifolds no longer form a heteroclinic connection. Instead, they form a *heteroclinic intersection* or *tangle* (see the cyan and brown curves in the top-left plot of Fig. 4). As a result, the map is not integrable, and an *exact invariant* $\mathcal{K}_4[p, q]$ satisfying

$$\mathcal{K}_4[p', q'] - \mathcal{K}_4[p, q] = 0,$$

for arbitrary q and p simply does not exist. The action variable can no longer be meaningfully defined — especially for large-amplitude dynamics. The rotation number as a function of position becomes a non-smooth function, exhibiting flat mode-locked regions (akin to the well-known Arnold tongues in the standard circle map [47–49] during parametric resonance). For even larger amplitudes, not only smoothness but also continuity of $\nu(J)$ breaks down, as the system transitions to fully chaotic motion with mixing [44]. Nevertheless, alongside fixed points, n -cycles, and their attached manifolds, the system still retains invariant structures, notably KAM tori (shown in black), which represent surviving regular orbits with irrational values of ν . So our goal is to construct, using only the equations of motion, an approximate function satisfying:

$$\mathcal{K}_4^{(n)}[p', q'] - \mathcal{K}_4^{(n)}[p, q] = \mathcal{O}(\epsilon^{n+1}).$$

In a preceding series of articles [50, 51], we explored connections between *integrable McMillan maps* [38, 52–54] and the chaotic Hénon map (and more broadly, *typical transformations in the McMillan form*). These approximations reproduce the dynamics up to the first order in J , and admit an approximate invariant:

$$\mathcal{K}_{4,a}^{(2)}[p, q] = p^2 - pq + q^2 - p^2q^2$$

corresponding to a map whose equations of motion agree with the Hénon system up to $\mathcal{O}(p^5)$

$$\begin{aligned} q' &= p, \\ p' &= -q + \frac{q}{1 - q^2} = -q + p + p^3 + \dots \end{aligned}$$

Notably, with the same nonlinear tune shift τ_0 at the origin, see the magenta curve labeled ν_a in the top-right plot of Fig. 4.

In the upcoming discussion, we address two important questions. (i) The first concerns how to systematically proceed to higher orders in such a way that, at a minimum, the twist coefficients τ_i are matched precisely. As we will discover, this question admits infinitely many solutions. The source of this indeterminacy lies in the fact that the invariant is only known up to an arbitrary function of itself, and, is directly related to the idea that the local dynamics within a simply connected region (or

within an infinitesimally small neighborhood of a fixed point, in the presence of chaos) can correspond to drastically different global systems. (ii) Although in our previous Hamiltonian examples a refinement was required to match the twist coefficient, in the current case — where τ_0 is already correctly reproduced — some further adjustment can still be made. Such refinement allows us to select among the infinitely many undetermined higher-order terms. For our case of the cubic Hénon map, an improved second-order approximate invariant takes the form:

$$\mathcal{K}_{4,b}^{(2)}[p, q] = p^2 - pq + q^2 - p^2 q^2 + \frac{7}{5}(p^2 - pq + q^2)^2.$$

The bottom row in Fig. 4 shows the level sets of both $\mathcal{K}_{4,a}^{(2)}[p, q]$ and $\mathcal{K}_{4,b}^{(2)}[p, q]$, while the top-right plot compares their respective $\nu(q)$ dependencies. For reference, it also includes the truncated power series expansion $\nu(q) = \nu_0 + (2\pi\sqrt{3})^{-1}q^2$ (orange), that can be derived via Lie transformations or expansions provided in [50]. Among the three approximations, the refined invariant $\mathcal{K}_{4,b}^{(2)}[p, q]$ gives the best estimate for the location of the unstable fixed point (marked with a red dot) and provides the best overall qualitative agreement. Before moving forward, it is worth noting that in systems exhibiting chaos, the size of the simply connected region obtained via approximations shrinks rapidly as one moves to higher orders. Consequently, low-order approximations often carry the most meaningful insights, capturing essential qualitative features of the system's behavior — features that tend to persist across a wide range of parameters and remain robust even when higher-order corrections become unreliable or analytically intractable.

B. Article Structure

Taking these considerations into account, we present our findings across two complementary articles. In the first article we focus on establishing the perturbative method and its technical foundations (Section II). As an illustrative example, we use a special *McMillan form* of the map, which offers great flexibility across different nonlinear mappings, while remaining symplectic and reversible. Our primary goal here is to verify convergence in an infinitesimally small neighborhood of the fixed point. This is done by comparing twist coefficients obtained via our method with those derived from the well-established Lie algebra technique (Subsection II E). To overcome the earlier-mentioned indeterminacy, we introduce the *averaging procedure* (Subsection II C). Interestingly, this transforms our perturbative approach into a *resonant theory*, i.e., one capable of handling situations where the rotation number is rational (commensurate with unity). This advancement allows us to handle diverging denominators (Subsection II D) and explains the rich structure of small-amplitude oscillations. This resonant capability is essential: in systems exhibiting nonlinear resonance, even infinitesimal amplitudes can produce behavior that contradicts traditional linearization techniques. We illustrate this by exploring both singular and

nonsingular low-order resonances in the quadratic and cubic Hénon maps.

Finally, to complete the technical description, Section III demonstrates how the method can be extended to general map forms and outlines a path toward applications in higher-dimensional systems. In the closing discussion, Section IV, we explore how our findings may offer new insights into the longstanding question of the size of stable KAM regions, particularly illuminating the remarkable stability observed in particle accelerators despite dramatic variations in their nonlinear optics designs.

In the second article, we turn to potential applications of the perturbative method by exploring large-amplitude dynamics. Here, we put our approach to a more demanding test: attempting to recover the global invariant in integrable mappings, where such invariants are known to exist. We demonstrate that, for McMillan integrable mappings with finite polynomial invariants, our perturbation theory converges exactly at the expected order. For mappings with infinite series invariants (such as the Suris trigonometric and exponential maps), our method appears to yield almost everywhere convergence, allowing the invariant to be recursively constructed. Having passed all critical benchmarks — accurate recovery of twist coefficients, correct treatment of rational rotation numbers, and convergence to known invariants — we move to potential applications. In particular, we attempt to reconstruct the behavior of the rotation number and a global invariant that captures dominant island structures. This analysis is carried out in an extended space of dynamical variables and mapping parameters, allowing for much broader coverage of possible regimes and avoiding the pitfall of being confined to specific phase space portraits. We conclude by comparing our method to the recently introduced Square Matrix (SM) technique [55–57]. As an example of a real-life application, we demonstrate how a single, moderately complex function (representing a low-order approximate invariant) can be used to reconstruct single particle dynamics across a range of seemingly unrelated accelerator facilities. Remarkably, this single expression captures essential nonlinear behavior in systems as different as the resonant extraction for Mu2e at the g-2 experiment, the Main Injector ring and the Integrable Optics Test Accelerator (IOTA) at Fermi-Lab. This unexpected unification underscores the power of low-order approximations in revealing shared structural dynamics across diverse machines.

Because this article benchmarks a broader body of prior research, it is important to mention several relevant auxiliary results. Articles [58–60] contain supporting material on the Danilov theorem, which helps bridge our perturbation theory with standard action-angle variables. The series [50, 51, 61] provides a detailed treatment of low-order integrable approximations. Article [19] offers a comprehensive explanation of the isochronous diagrams used in the second part of this study. Finally, we acknowledge the foundational review of reversibility in dynamical systems by Roberts and Quispel [18].

II. PERTURBATION THEORY

In this section, we develop a method to construct an approximate invariant of motion for (quasi-) nearly integrable orbits governed by a symplectic map, $T : \zeta \mapsto \zeta'$, defined on the plane $\zeta = (q, p) \in \mathbb{R}^2$, and which can be expressed in the so called *McMillan form* [18, 38, 39, 41, 42, 50–54]:

$$\begin{aligned} T : \quad q' &= p, \\ p' &= -q + f(p), \end{aligned} \quad (2)$$

where $f(p)$ is a C^∞ function referred to as the *force function*, or simply *force*. While T may not exhibit global quasi-integrability, we assume the existence of invariant KAM tori in the neighborhood of a fixed point [1–3].

The map is reversible [16–19], and therefore, along with its inverse, it can be expressed as a composition of two involutory, anti-area-preserving transformations, called *reversors*:

$$T = R_2 \circ R_1, \quad T^{-1} = R_1 \circ R_2, \quad R_{1,2}^2 = \text{Id},$$

where

$$\begin{aligned} R_1 : \quad q' &= p, & R_2 : \quad q' &= q, \\ p' &= q, & p' &= -p + f(q). \end{aligned}$$

The first reversor, $R_1 = \text{Ref}(\pi/4)$, corresponds to a linear reflection with respect to the main diagonal, where

$$\text{Ref}(\theta) = \begin{bmatrix} \cos(2\theta) & \sin(2\theta) \\ \sin(2\theta) & -\cos(2\theta) \end{bmatrix}.$$

The second reversor performs a vertical reflection about the line $p = f(q)/2$. These lines, known as *symmetry lines* or simply *symmetries* of T , correspond to the fixed-point sets of the reversors:

$$l_1 = \text{Fix}(R_1) : p = q, \quad l_2 = \text{Fix}(R_2) : p = f(q)/2.$$

If any point of an orbit belongs to $\mathcal{M}_n = \text{Fix}(T^n R_{1,2})$, the orbit is termed *symmetric*. Otherwise, it is referred to as *asymmetric*. Points that belong to $\mathcal{M}_{m,n} = \mathcal{M}_m \cap \mathcal{M}_n$ are called *doubly symmetric*. It follows that [16, 17]: (i) every doubly symmetric point is periodic under T , and (ii) every symmetric periodic point is doubly symmetric. In particular, all fixed points of the system, $\zeta^{(1)} = T \zeta^{(1)}$, and 2-cycles, $\zeta^{(2)} = T^2 \zeta^{(2)}$, are given as intersections of l_1 and $l_2^{\pm 1}$, respectively:

$$\zeta^{(1)} : \begin{cases} p = q, \\ p = f(q)/2, \end{cases} \quad \text{and} \quad \zeta^{(2)} : \begin{cases} q = f(p)/2, \\ p = f(q)/2. \end{cases}$$

In the following derivations, we will assume, without loss of generality, that at least one fixed point is located at the origin. This can always be achieved by a constant shift of coordinates $(q, p) \rightarrow (q, p) + \lambda(1, 1)$, where λ is

chosen such that $f(0) = 0$. The linear stability of this fixed point is defined by the trace of its Jacobian matrix:

$$dT(\zeta) = \begin{bmatrix} \frac{\partial q'}{\partial q} & \frac{\partial q'}{\partial p} \\ \frac{\partial p'}{\partial q} & \frac{\partial p'}{\partial p} \end{bmatrix} = \begin{bmatrix} 0 & 1 \\ -1 & \partial_p f(p) \end{bmatrix},$$

where the condition $|\text{tr} dT(\mathbf{0})| < 2$, gives the stability criterion:

$$|a| < 2, \quad a = \partial_p f(0),$$

with a being related to the *bare/unperturbed rotation number*:

$$\nu_0 = \arccos[a/2]/(2\pi).$$

Next, any set of points Γ is called *invariant* under T , if:

$$T\Gamma = \Gamma. \quad (3)$$

If the mapping is integrable, it should possess an *exact invariant of motion* $\mathcal{K}[p, q]$, such that for any point of the plane $\zeta \in \mathbb{R}^2$ and its image ζ' :

$$\mathcal{K}[\zeta'] - \mathcal{K}[\zeta] = 0. \quad (4)$$

As noted by E. McMillan [38], the constant level set of such an invariant is not only invariant under T , Eq. (3), but must also be invariant under both reflections:

$$\mathcal{K}[R_1\zeta] - \mathcal{K}[\zeta] = 0, \quad \mathcal{K}[R_2\zeta] - \mathcal{K}[\zeta] = 0. \quad (5)$$

Thus, in general, the constant level set of the invariant of a reversible mapping, $\mathcal{K}[p, q] = \text{const}$, consists of symmetric invariant subsets and pairs of asymmetric invariant subsets [18]. This makes the invariance condition (4) more general than (3), as the entire union $\mathcal{K}[p, q] = \text{const}$ must necessarily satisfy (5).

To develop a perturbation theory, we introduce a small positive parameter, ϵ , to characterize the amplitude of oscillations. This can be achieved by performing a change of variables, $(q, p) \rightarrow \epsilon(q, p)$. Under this transformation, the map (2) retains its original form, with the force function modified as follows:

$$f(p) \rightarrow \frac{f(\epsilon p)}{\epsilon} = ap + \epsilon bp^2 + \epsilon^2 cp^3 + \epsilon^3 dp^4 + \dots,$$

where $f(p)$ is expanded into a power series

$$b \equiv \frac{\partial_p^2 f(0)}{2!}, \quad c \equiv \frac{\partial_p^3 f(0)}{3!}, \quad d \equiv \frac{\partial_p^4 f(0)}{4!}, \quad e \equiv \frac{\partial_p^5 f(0)}{5!}.$$

Finally, as we will observe, enforcing the first symmetry $p = q$ is essential, prompting the introduction of the following notations:

$$\Sigma = p + q, \quad \Pi = pq,$$

along with their combination

$$\text{C.S.} = \Sigma^2 - (2 + a)\Pi = p^2 - apq + q^2,$$

corresponding to the zeroth-order (linearized) invariant, commonly known as the *Courant-Snyder invariant* [20], and playing a significant role in the expansion.

A. Approximate invariant of motion

After introducing ϵ , we construct a perturbation theory in which, at each order n , we seek an *approximate invariant*, assumed to take the form of a power series

$$\mathcal{K}^{(n)}[p, q] = \mathcal{K}_0 + \epsilon \mathcal{K}_1 + \epsilon^2 \mathcal{K}_2 + \dots + \epsilon^n \mathcal{K}_n$$

and conserved up to an accuracy of $\mathcal{O}(\epsilon^{n+1})$:

$$\mathcal{R}_n \equiv \mathcal{K}^{(n)}[p', q'] - \mathcal{K}^{(n)}[p, q] = \mathcal{O}(\epsilon^{n+1}), \quad (6)$$

where \mathcal{R}_n is referred to as the *residual of an approximate invariant*, or simply the *residual*. To obtain the general solution, we adopt an ansatz where each \mathcal{K}_m is a polynomial of degree $(m+2)$ with terms of equal powers in p and q :

$$\begin{aligned} \mathcal{K}_0 &= C_{2,0} p^2 + C_{1,1} p q + C_{0,2} q^2, \\ \mathcal{K}_1 &= C_{3,0} p^3 + C_{2,1} p^2 q + C_{1,2} p q^2 + C_{0,3} q^3, \\ \mathcal{K}_2 &= C_{4,0} p^4 + C_{3,1} p^3 q + C_{2,2} p^2 q^2 + C_{1,3} p q^3 + C_{0,4} q^4, \\ &\dots \end{aligned}$$

Here, $C_{i,j}$ are coefficients to be determined by satisfying Eq. (6). At first glance, this approach seems to require solving for $(m+3)$ coefficients for each \mathcal{K}_m . However, by using the following three propositions — each straightforward to verify — we show that the number of coefficients defined by Eq. (6) is reduced to $\lfloor (m+1)/2 \rfloor$.

Proposition 1 *For the mapping in the form (2), \mathcal{R}_n is of order $\mathcal{O}(\epsilon^{n+1})$ only if $C_{i,j} = C_{j,i}$.*

This implies that the first symmetry, $\mathcal{K}[p, q] = \mathcal{K}[q, p]$, is inherently satisfied, while Eq. (4) provides a quantitative measure of the extent to which the second symmetry is upheld:

$$\begin{aligned} \mathcal{K}^{(n)}[p', q'] - \mathcal{K}^{(n)}[p, q] &= \mathcal{K}^{(n)}[q', p'] - \mathcal{K}^{(n)}[p, q] = \\ &= \mathcal{K}^{(n)}[p, -q + f(p)] - \mathcal{K}^{(n)}[p, q]. \end{aligned}$$

Consequently, we express the expansion as follows for even and odd orders, respectively, with $m \geq 0$:

$$\begin{aligned} \mathcal{K}_{2m} &= \sum_{j=0}^{m+1} B_{m+1-j,j} \Pi^{m+1-j} \text{C.S.}^j, \\ \mathcal{K}_{2m+1} &= \sum_{j=0}^{m+1} A_{m+1-j,j} \Pi^{m+1-j} \text{C.S.}^j \Sigma. \end{aligned}$$

Proposition 2 *For the mapping in the form (2), \mathcal{R}_n is of order $\mathcal{O}(\epsilon^{n+1})$ only if all coefficients of terms proportional to $\Sigma \text{C.S.}^j$ and $\Pi \text{C.S.}^j$ vanish:*

$$\forall j: \quad A_{0,j} = 0, \quad B_{1,j} = 0.$$

Proposition 3 *If an even polynomial $\mathcal{K}^{(2n)}[p, q]$ satisfies*

$$\mathcal{K}^{(2n)}[p', q'] - \mathcal{K}^{(2n)}[p, q] = \mathcal{O}(\epsilon^{2n+1}),$$

for the map (2), then the modified polynomial

$$\mathcal{K}^{(2n)}[p, q] + \epsilon^{2n} C_n \text{C.S.}^{n+1}$$

also satisfies this condition for any value of C_n .

With these propositions in hand, we now look for the solution in the form:

$$\begin{aligned} \mathcal{K}_0 &= C_0 \text{C.S.} \\ \mathcal{K}_1 &= A_1^1 \Pi \Sigma \\ \mathcal{K}_2 &= B_1^1 \Pi^2 + C_1 \text{C.S.}^2 \\ \mathcal{K}_3 &= A_2^2 \Pi^2 \Sigma + A_2^1 \Pi \Sigma \text{C.S.} \\ \mathcal{K}_4 &= B_2^2 \Pi^3 + B_2^1 \Pi^2 \text{C.S.} + C_2 \text{C.S.}^3 \\ \mathcal{K}_5 &= A_3^3 \Pi^3 \Sigma + A_3^2 \Pi^2 \Sigma \text{C.S.} + A_3^1 \Pi \Sigma \text{C.S.}^2 \\ &\dots, \end{aligned}$$

where the coefficients are defined using the final notations:

$$A_i^j \equiv A_{j,i-j}, \quad B_i^j \equiv B_{j+1,i-j}, \quad C_i \equiv B_{0,i+1}.$$

Thus, at the n -th order, we determine the coefficients by independently setting to zero all combined multipliers of the terms $p^k q^l \epsilon^{k+l-2}$ in Eq. (6), where $k+l-2 \leq n$. According to the last proposition, the resulting system is overdetermined, allowing only the coefficients A_i^j and B_i^j to be uniquely determined. In contrast, the coefficients C_i cannot be determined without introducing additional constraints. Remarkably, Eq. (6) is satisfied to the appropriate order regardless of the specific values of C_i .

To understand the nature of C_i , recall that if $\mathcal{K}[p, q]$ is an exact invariant of the map T , then any function of $\mathcal{K}[p, q]$ is also an invariant. For instance, in the case of a linear map $f(p) = a p$ with the invariant

$$\mathcal{K}_0[p, q] = \text{C.S.},$$

any power series in C.S. (whether finite, infinite, or simply scaled by a constant) remains an invariant:

$$C_0 \text{C.S.} + C_1 \text{C.S.}^2 + C_2 \text{C.S.}^3 + \dots$$

Next, consider the symmetric McMillan map [38, 50–54] with

$$f_{\text{SM}}(p) = -\frac{\beta p - a}{\alpha p^2 + \beta p + 1} p$$

and the corresponding invariant

$$\mathcal{K}_{\text{SM}}[p, q] = \text{C.S.} + \beta \Pi \Sigma + \alpha \Pi^2.$$

Examining a series of the form

$$C_0 \mathcal{K}_{\text{SM}} + C_1 \mathcal{K}_{\text{SM}}^2 + C_2 \mathcal{K}_{\text{SM}}^3 + \dots$$

and retaining terms up to ϵ^2 , we obtain

$$C_0 \mathcal{K}_{\text{SM}} + C_1 \text{C.S.}^2 + \dots$$

It follows that the specific values of C_i do not affect intrinsic dynamical properties such as the rotation number ν_0 or the twist coefficient $\tau_0 = (d\nu/dJ)_{J=0}$.

B. Perturbation theory at lower orders

To begin, we derive exact expressions for the coefficients A_i^j and B_i^j in the lower orders of the perturbation theory. As a first step, we examine the zeroth-order approximate invariant:

$$\mathcal{K}^{(0)} = C_0 \text{C.S.},$$

where C_0 is referred to as the *seed coefficient*. For simplicity, we set the seed to unity, $C_0 = 1$, since all higher-order terms are proportional to C_0 . This choice will later be revisited in the next subsection, which addresses the removal of singularities.

Using the iterative procedure of setting the multipliers in Eq. (6) to zero for $n > 0$, we calculate the approximate invariant up to the third order:

$$\mathcal{K}^{(3)} = \mathcal{K}_0 + \epsilon \mathcal{K}_1 + \epsilon^2 \mathcal{K}_2 + \epsilon^3 \mathcal{K}_3 \quad (7)$$

where the terms are given by:

$$\begin{aligned} \mathcal{K}_1 &= -\frac{b}{r_3} \Pi \Sigma, \\ \mathcal{K}_2 &= \frac{b^2 - r_3 c}{r_3 r_4} \Pi^2 + C_1 \text{C.S.}^2, \\ \mathcal{K}_3 &= \frac{\mathcal{T}_0}{r_3 r_4 r_5} \left[\Pi^2 \Sigma - \frac{\Pi \Sigma \text{C.S.}}{r_3} \right] + 2b C_1 \frac{\Pi \Sigma \text{C.S.}}{r_3}, \\ \mathcal{T}_0 &= b^3 - (r_3 + r_4) b c + r_3 r_4 d. \end{aligned}$$

For completeness, the next-order terms are provided in Appendix A 2. In deriving the expressions above, we introduced the following notations for resonant terms (see Table I for details):

$$r_k = \prod_l (a - a_{\nu_l}), \quad a_{\nu_l} = 2 \cos(2\pi \nu_l), \quad \nu_l = l/k,$$

where the product runs over indices l such that ν_l are irreducible fractions with denominator k :

$$l : \text{gcd}(l, k) = 1 \quad \text{and} \quad 0 \leq \nu_l \leq 1/2.$$

A dynamical system is said to be on the k -th order resonance when one of the conditions $r_k = 0$, is satisfied.

C. Averaging procedure

After determining all A_i^j and B_i^j , we now discuss the choice of the coefficients C_i , using C_1 as an illustrative example. From the last proposition, we know that at each order, the residual \mathcal{R}_n is of the order $\mathcal{O}(\epsilon^{n+1})$, regardless of the choice of C_i . This suggests that we should consider the next-order terms in the residual:

$$\mathcal{R}_n = \overline{\mathcal{R}_n} \epsilon^{n+1} + \overline{\overline{\mathcal{R}_n}} \epsilon^{n+2} + \mathcal{O}(\epsilon^{n+3}).$$

k	ν_l	a_{ν_l}	r_k
1	0	2	$a - 2$
2	1/2	-2	$a + 2$
3	1/3	-1	$a + 1$
4	1/4	0	a
5	1/5	$(-1 + \sqrt{5})/2$	$a^2 + a - 1$
	2/5	$(-1 - \sqrt{5})/2$	
6	1/6	1	$a - 1$
7	1/7	$2 \cos(2\pi/7)$	$a^3 + a^2 - 2a - 1$
	2/7	$2 \cos(4\pi/7)$	
	3/7	$2 \cos(6\pi/7)$	
8	1/8	$\sqrt{2}$	$a^2 - 2$
	3/8	$-\sqrt{2}$	
9	1/9	$2 \cos(2\pi/9)$	$a^3 - 3a + 1$
	2/9	$2 \cos(4\pi/9)$	
	4/9	$2 \cos(8\pi/9)$	
10	1/10	$(1 + \sqrt{5})/2$	$a^2 - a - 1$
	3/10	$(1 - \sqrt{5})/2$	

TABLE I. Resonant rotation numbers ν_l , their corresponding trace values a_{ν_l} , and, the resonant terms r_k for resonance orders $k \leq 10$.

The coefficient C_1 first appears in the second order ($n = 2$) of the approximate invariant Eq. (7). The corresponding ϵ^3 terms in the residual \mathcal{R}_2 are given by:

$$\overline{\mathcal{R}_2}[p, q] = (ap - 2q) p^2 \left[\frac{\mathcal{T}_0}{r_3 r_4} p^2 + 2b C_1 \text{C.S.} \right].$$

From this expression, it is evident that no choice of C_1 can entirely eliminate $\overline{\mathcal{R}_2}$. Therefore, instead of seeking to nullify it, we aim to minimize its variation.

To achieve this, we perform a canonical transformation of the phase-space variables to Floquet coordinates, defined as:

$$\begin{aligned} (q, p) \mapsto (J, \phi) : \quad q/\sqrt{2J} &= \delta \cos \phi + \frac{a}{2\delta} \sin \phi, \\ p/\sqrt{2J} &= \delta^{-1} \sin \phi, \end{aligned}$$

and where

$$\delta = \sqrt{\sin(2\pi \nu_0)} = (1 - a^2/4)^{1/4}.$$

In these coordinates, the C.S. term simplifies to a form independent of φ

$$\text{C.S.} = \sqrt{4 - a^2} J,$$

while $\overline{\mathcal{R}_n}[J, \varphi]$ becomes a periodic function of φ . For example, the expression for $\overline{\mathcal{R}_2}[J, \varphi]$ is:

$$\begin{aligned} \overline{\mathcal{R}_2}[J, \varphi] &= 8(-r_1 r_2)^{1/4} \sin(\varphi) \sin(2\varphi) J^{5/2} \times \\ &\times \left[\frac{2\mathcal{T}_0}{r_1 r_2 r_3 r_4} \sin^2(\varphi) - b C_1 \right]. \end{aligned}$$

Since the phase average of $\overline{\mathcal{R}_2}[J, \varphi]$ vanishes:

$$\int_0^{2\pi} \overline{\mathcal{R}_n}[J, \varphi] d\varphi = 0,$$

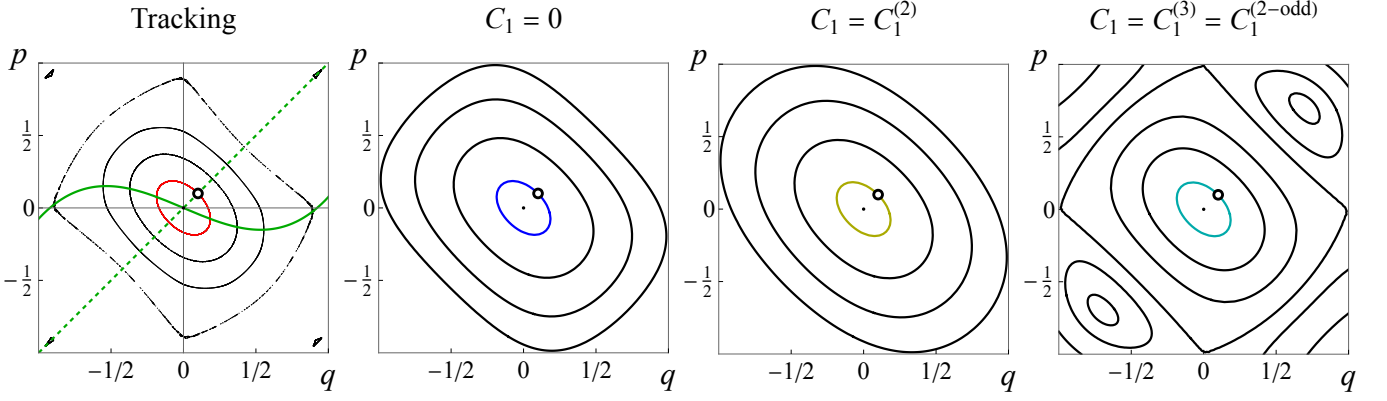


FIG. 5. The left plot depicts phase-space trajectories of the cubic map $f(p) = ap + p^3$ for $a = -17/20$, obtained through numerical tracking. A sample orbit ζ_0 , corresponding to the initial condition $(q_0, p_0) = (1/10, 1/10)$ (marked as a white point), is highlighted in red. Green curves are the first $p = q$ (dashed) and second $p = f(q)/2$ (solid) symmetry lines. The subsequent three plots illustrate the constant level sets of the approximate invariant $\mathcal{K}^{(2)}[p, q]$ for different values of the coefficient C_1 . The case $C_1 = 0$ represents an integrable approximation via the canonical McMillan map. The next case with $C_1 = C_1^{(2)}$ demonstrates an “incorrect” averaging at order ϵ^3 . The last plot corresponds to the averaging at order ϵ^4 , yielding the invariant $\langle \mathcal{K}_{\text{odd}}^{(2)}[p, q] \rangle$. In each plot, the level set passing through the point ζ_0 is highlighted for clarity.

we minimize the integral of its square:

$$I_n = \int_0^{2\pi} \overline{\mathcal{R}_n}^2[J, \varphi] d\varphi$$

by solving for the coefficients C_k using the system of linear equations:

$$\frac{d}{dC_k} I_n = 0.$$

For the second order ($n = 2$), this procedure yields:

$$C_1^{(2)} = \frac{5}{4b} \frac{\mathcal{T}_0}{r_1 r_2 r_3 r_4}. \quad (8)$$

This *averaging procedure* is repeated at each order of the perturbation theory. The superscript notation indicates the order n for which the coefficient is determined. For example, at $n = 3$, only $C_1^{(3)}$ is involved, and it is computed by solving $dI_3/dC_1 = 0$. At $n = 4$, the system of two linear equations $dI_4/dC_{1,2} = 0$ provides the values of $C_{1,2}^{(4)}$. Exact expressions for higher-order coefficients are provided in Appendix A 3.

When the force is an odd function, $f(-p) = -f(p)$:

$$f_{\text{odd}}(p) = ap + cp^3 + ep^5 + gp^7 + \dots,$$

the expansion of $\mathcal{K}^{(n)}$ involves only even powers of ϵ , yielding the following expression for the first two nonlinear orders:

$$\begin{aligned} \mathcal{K}_{\text{odd}}^{(n)}[p, q] &= \mathcal{K}_0 + \epsilon^2 \mathcal{K}_2 + \epsilon^4 \mathcal{K}_4 + \dots = \\ &= \text{C.S.} - \frac{c}{r_4} \Pi^2 \epsilon^2 + C_1 \text{C.S.}^2 \epsilon^2 + C_2 \text{C.S.}^3 \epsilon^4 + \\ &+ \left[\frac{c^2 - r_4 e}{r_3 r_4 r_6} \left(\Pi - \frac{\text{C.S.}}{r_4} \right) - 2c C_1 \frac{\text{C.S.}}{r_4} \right] \Pi^2 \epsilon^4 + \dots \end{aligned}$$

In this case, all $\overline{\mathcal{R}_n} = 0$, so the leading-order contributions to the residual come from ϵ^{n+2} terms, specifically $\overline{\mathcal{R}_n}$. For $n = 2$, we have

$$\begin{aligned} \overline{\mathcal{R}_2}[J, \varphi] &= 16 \sin^2(\varphi) \sin(2\varphi) J^3 \times \\ &\times \left[2 \frac{r_4 e - c^2}{r_1 r_2 r_4} \sin^2(\varphi) - c C_1 \right], \end{aligned}$$

which allows us to obtain

$$C_1^{(2-\text{odd})} = \frac{7}{5c} \frac{r_4 e - c^2}{r_1 r_2 r_4} : \quad \frac{dI_2^{\text{odd}}}{dC_1} = 0, \quad (9)$$

where

$$I_n^{\text{odd}} = \int_0^{2\pi} \overline{\mathcal{R}_n}^2[J, \varphi] d\varphi.$$

Notice that, since the averaging was performed over ϵ^4 terms, Eq. (9) cannot be obtained as a limiting case $b, d = 0$ of the general expansion $C_1^{(2)}$, Eq. (8). Instead, it arises from applying the same limit to $C_1^{(3)}$, see Appendix A 3.

Figs. 5 and 6 illustrate the impact of different choices of C_1 on the cubic Hénon map, given by $f = ap + p^3$ with $a = -17/20$. The first set of figures compares the trajectory of a sample orbit, initialized at $\zeta_0 = 10^{-1}(1, 1)$ (shown in red in the left plot), with the level sets of the approximate invariant of second order $\mathcal{K}^{(2)}[\zeta_0]$. The second plot in Fig. 5 corresponds to $C_1 = 0$, representing the approximation via the integrable McMillan map. The third graph illustrates the effect of an “incorrect” averaging, while the fourth shows the case for $C_1 = C_1^{(2-\text{odd})}$. Fig. 6 further demonstrates the conservation of the approximate invariant along the sample orbit, with the average value subtracted to allow for a clearer comparison. As observed, the choice $C_1 = C_1^{(3)} = C_1^{(2-\text{odd})}$ provides the most accurate results.

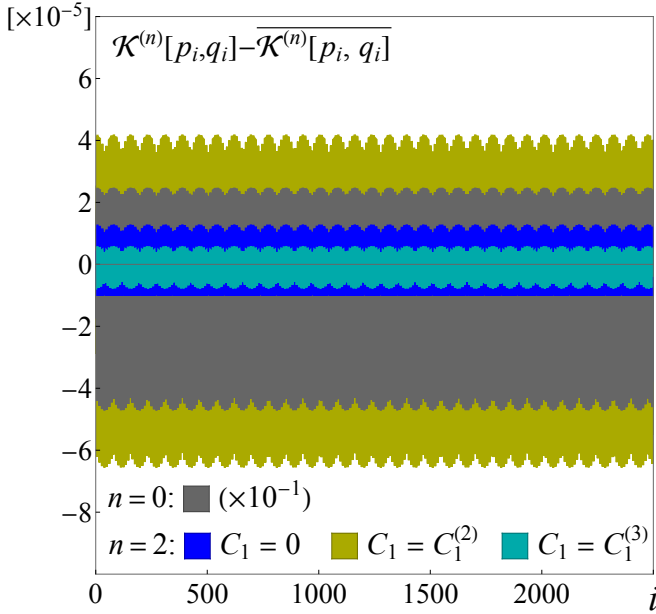


FIG. 6. The approximate invariant $\mathcal{K}^{(n)}[p_i, q_i]$, evaluated along the sample orbit $(q_0, p_0) = (1/10, 1/10)$ for the cubic map $f(p) = ap + p^3$ with $a = -17/20$, is shown as a function of the number of iterations i . The vertical axis is scaled by a factor of $\times 10^{-5}$ for clarity. Different colors represent $n = 0$ and $n = 2$ for various choices of the coefficient C_1 , as detailed in Fig. 5. For each case, the average value of the evaluated invariant is subtracted to facilitate direct comparison.

After determining the coefficients C_i , we define, at each order, an *averaged approximate invariant*:

$$\langle \mathcal{K}^{(n)} \rangle = \mathcal{K}^{(n)}(C_k : dI_n/dC_k = 0).$$

For $n = 2$, this results in:

$$\begin{aligned} \langle \mathcal{K}^{(2)} \rangle[p, q] &= \text{C.S.} - \frac{b}{r_3} \Pi \Sigma \epsilon + \\ &+ \left[\frac{b^2 - r_3 c}{r_3 r_4} \Pi^2 + \frac{5}{4b} \frac{\mathcal{T}_0}{r_1 r_2 r_3 r_4} \text{C.S.}^2 \right] \epsilon^2, \\ \langle \mathcal{K}_{\text{odd}}^{(2)} \rangle[p, q] &= \text{C.S.} - \left[\frac{c}{r_4} \Pi^2 + \frac{7}{5c} \frac{c^2 - r_4 e}{r_1 r_2 r_4} \text{C.S.}^2 \right] \epsilon^2. \end{aligned}$$

Before moving to the next subsection, we present two observations worth mentioning.

Observation #1. Odd mappings in the McMillan form exhibit *double reversibility* because they commute with the area-preserving involution [18, 19]:

$$T_{\text{odd}} = \text{Rot}(\pi) \circ T_{\text{odd}} \circ \text{Rot}^{-1}(\pi).$$

This property gives rise to a class of transformations distinct from $R_{1,2}$, such that:

$$T_{\text{odd}} = Q_2 \circ Q_1, \quad T_{\text{odd}}^{-1} = Q_1 \circ Q_2, \quad Q_{1,2}^2 = \text{Id},$$

where $Q_1 = R_1 \circ \text{Rot}(\pi) = \text{Rot}(3\pi/4)$ and $Q_2 = T_{\text{odd}} \circ Q_1$,

$$\begin{aligned} Q_1 : q' &= -p, & Q_2 : q' &= -q, \\ p' &= -q, & p' &= p - f_{\text{odd}}(q). \end{aligned}$$

The transformations $Q_{1,2}$ form an independent group of symmetries, introducing two additional symmetry lines:

$$l_3 = \text{Fix}(Q_1) : p = -q, \quad l_4 = \text{Fix}(Q_2) : q = 0.$$

It is worth noting that the absence of odd powers of ϵ in $\mathcal{K}_{\text{odd}}^{(n)}$ enforces symmetry along l_3 at each order. Thus, double reversibility offers an additional constraint that can be utilized in determining the approximate invariant.

Observation #2. As a result of choosing $C_0 = 1$, both $\mathcal{K}^{(n)}$ and $\langle \mathcal{K}^{(n)} \rangle$ contain singular terms with denominators that vanish at certain resonant values of $a_{\nu_j} : r_j = 0$. Before averaging, some terms in $\mathcal{K}^{(n)}$ involve denominators proportional to r_j^m where $m > 1$. However, after applying the averaging procedure and substituting all C_i , the powers of these terms appear to reduce to $m = 1$ in all orders. Consequently, $\langle \mathcal{K}^{(n)} \rangle$ can be expressed as:

$$\langle \mathcal{K}^{(n)} \rangle = \frac{1}{r_1 r_2 \dots r_{n+2}} \left(\dots \right),$$

where the terms inside the parentheses do not introduce singularities at rational values of ν_0 .

D. Removal of singularities

Since r_j are independent of the dynamical variables, we can choose C_0 to be the product of all singular denominators that appear in the expressions. Thus, we define *non-singular* averaged invariants:

$$\{ \mathcal{K}^{(n)} \} = \langle \mathcal{K}^{(n)} \rangle \prod_{k=1}^{n+2} r_k.$$

For instance, compare the following with the previously derived results for $n = 2$:

$$\begin{aligned} \{ \mathcal{K}^{(2)} \}[p, q] &= r_1 r_2 r_3 r_4 \text{C.S.} - r_1 r_2 r_4 b \Pi \Sigma \epsilon + \\ &+ \left[r_1 r_2 (b^2 - r_3 c) \Pi^2 + \frac{5}{4} \frac{\mathcal{T}_0}{b} \text{C.S.}^2 \right] \epsilon^2, \\ \{ \mathcal{K}_{\text{odd}}^{(2)} \}[p, q] &= r_1 r_2 r_4 \text{C.S.} - \\ &- \left[r_1 r_2 c \Pi^2 + \frac{7}{5} \frac{c^2 - r_4 e}{c} \text{C.S.}^2 \right] \epsilon^2. \end{aligned}$$

In this new form, when the resonance condition $r_j = 0$ is met, the previously singular terms now define the shape of the invariant, while all other terms effectively vanish due to the corresponding multiplier r_j .

Observation #3. As we proceed to higher orders, it becomes evident that, right at resonance $r_j = 0$, lower-order terms proportional to C.S.^m , including $m = 1$, can vanish. This is an important property that perturbation theory should exhibit, as in nonlinear systems, a zeroth-order linearized invariant C.S. may be an inadequate approximation, even for infinitesimally small amplitudes.

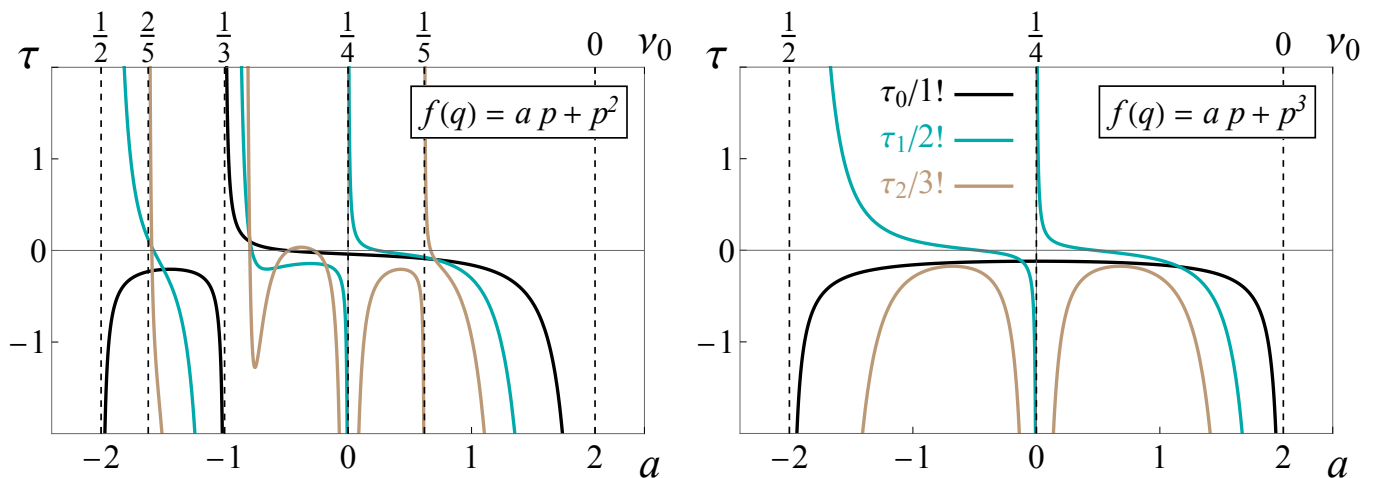


FIG. 7. First three twist coefficients $\tau_{0,1,2}$ for the Hénon quadratic ($f(p) = ap + p^2$) and cubic ($f(p) = ap + p^3$) mappings. The linear scale at the bottom provides the trace of the Jacobian at the origin, a , while the scale at the top shows corresponding values of the bare rotation number, ν_0 , defined for $|a| \leq 2$.

Before presenting examples, let us recall that in Birkhoff normal form theory (see, e.g., [45]) the map's *canonical form* is given by

$$\begin{aligned} J' &= J, \\ \theta' &= \theta + 2\pi\nu(J), \end{aligned} \quad (10)$$

where J is the *action* (or *symplectic radius*) and θ is its *conjugate angle* variables. The rotation number is often expanded as a power series in the action:

$$\nu(J) = \nu_0 + \tau J = \nu_0 + \tau_0 J + \frac{1}{2!} \tau_1 J^2 + \frac{1}{3!} \tau_2 J^3 + \mathcal{O}(J^4),$$

where its derivative, known as the *twist*, is given by

$$\tau(J) = \frac{d\nu}{dJ} = \tau_0 + \tau_1 J + \frac{1}{2} \tau_2 J^2 + \mathcal{O}(J^3).$$

The coefficients τ_i are called *twist coefficients*. For McMillan-form mappings (2) with a smooth force, the first twist coefficient τ_0 is expressed as:

$$2\pi\tau_0 = \frac{1}{r_1 r_2} \left[3c - 4 \frac{a + 1/2}{r_1 r_3} b^2 \right]. \quad (11)$$

When $b \neq 0$, τ_0 is well-defined except at $\nu_0 = 0, 1/2, 1/3$ (i.e., $a = 2, -2, -1$), where it becomes singular. Additionally, $\tau_{1,2}$ is only defined for $\nu_0 \neq 1/4, 1/5, 2/5$ (i.e., $a \neq 0, (-1 \pm \sqrt{5})/2$). Expressions for τ_1 and τ_2 are provided at the end of this article, Eqs. (A2) and (A3), while Fig. 7 illustrates $\tau_{0,1,2}(a)$ for the Hénon quadratic and cubic maps, which we will use in our examples. While these results can be derived using various methods — such as Birkhoff normal forms [45], Lie algebra techniques [24, 25], square matrix method [62], or Deprit perturbation theory [63] — recent studies [50, 51] have demonstrated that τ_0 can also be obtained from expansions of the action variable in integrable McMillan multipoles. This provides additional qualitative insights and serves as a useful tool for further discussions.

1. Quarter integer resonance

As our first example, we examine the quarter-integer resonance $\nu_0 = 1/4$ at $a = 0$. For both the quadratic and cubic maps, the first twist coefficient remains finite:

$$\tau_0[b = 1, c = 0] = -\frac{1}{8\pi}, \quad \tau_0[b = 0, c = 1] = -\frac{3}{8\pi}.$$

This ensures that the nonlinear resonance is stable, leading to the formation of a characteristic chain of four islands for $\nu_0 > \nu_r$, as shown in cases (a.) and (b.) of Fig. 8. Meanwhile, in the general case $b^2 \neq c$, higher-order twist coefficients become singular.

In the vicinity of the resonance, $\delta_r = \nu_r - \nu_0 \approx 0$, one might naively expect small-amplitude invariant curves described by

$$\text{C.S.}[a = 0] = p^2 + q^2.$$

However, a closer inspection reveals a more intricate picture. For the Hénon quadratic map at exact resonance $\nu_0 = 1/4$, phase space trajectories exhibit cross-like structures, as seen in Fig. 8 (b.). In contrast, zooming in on the region near the origin for slightly off-resonant cases ($\delta_r \neq 0$) reveals circular trajectories, consistent with expectations. A similar phenomenon occurs in the cubic map: when on the resonance, the trajectories form more square-like invariant structures rather than circular ones, as shown in Fig. 8 (a.). To better understand these emergent shapes, we turn to perturbation theory and examine the first few orders of the expansion. After averaging and eliminating singular terms, we obtain the following expressions for the case $c = 1$, up to a constant multiplier:

$$\begin{aligned} \{\mathcal{K}_{c=1}^{(2)}\} &= \left(\Pi^2 - \frac{7}{10} \frac{\text{C.S.}^2}{2} \right) \epsilon^2, \\ \{\mathcal{K}_{c=1}^{(4)}\} &= \left(\Pi^2 - \frac{\text{C.S.}^2}{2} \right) \epsilon^2 + \Pi^3 \epsilon^4. \end{aligned}$$

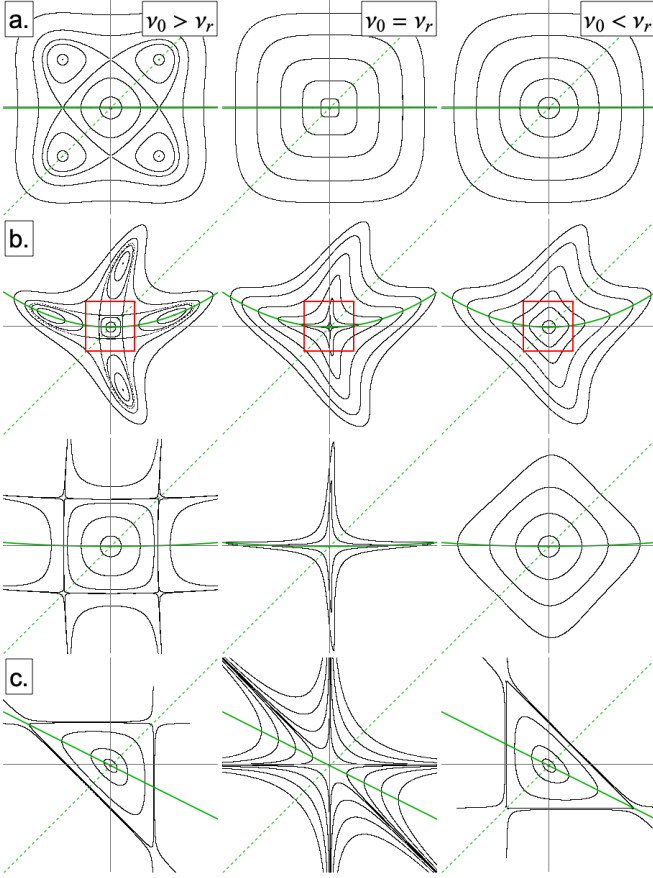


FIG. 8. Phase space morphology across low-order resonances. The top rows show the 4-island chain bifurcation $\nu_r = 1/4$ for the Hénon (a.) cubic $f(p) = ap + p^2$ and (b.) quadratic $f(p) = ap + p^3$ maps. The third row provides a magnified view of the regions highlighted in red. The last row (c.) depicts the touch-and-go bifurcation in the quadratic map, $\nu_r = 1/3$. Green curves are the first (dashed) and second (solid) symmetry lines.

As we proceed, we observe that the coefficients provided by $\{\mathcal{K}_{c=1}^{(4)}\}$ converge:

$$\{\mathcal{K}_{c=1}^{(n \geq 6)}\} = \left(\Pi^2 - \frac{\text{C.S.}^2}{2} \right) \epsilon^2 + \Pi^3 \epsilon^4 + \mathcal{O}(\epsilon^6). \quad (12)$$

The first term ($\propto \epsilon^2$) now matches precisely the trajectories for infinitesimally small amplitudes. The corresponding shape is shown in Fig. 9, (a.1). Since this leading-order term already defines a stable (closed) level set, the addition of the next-order term, proportional to ϵ^3 , does not alter the shape in the limit $q, p \rightarrow 0$, case (a.2).

Returning to the case of the quadratic map, we obtain the following sequence of approximations:

$$\{\mathcal{K}_{b=1}^{(1)}\} = \text{C.S.} - \Pi \Sigma \epsilon,$$

$$\{\mathcal{K}_{b=1}^{(2)}\} = \left(\Pi^2 - \frac{5 \text{C.S.}^2}{8} \right) \epsilon^2,$$

$$\{\mathcal{K}_{b=1}^{(3)}\} = \left(\Pi^2 - \frac{34 \text{C.S.}^2}{69} \right) \epsilon^2 + \left(\Pi - \frac{35}{69} \text{C.S.} \right) \Pi \Sigma \epsilon^3$$

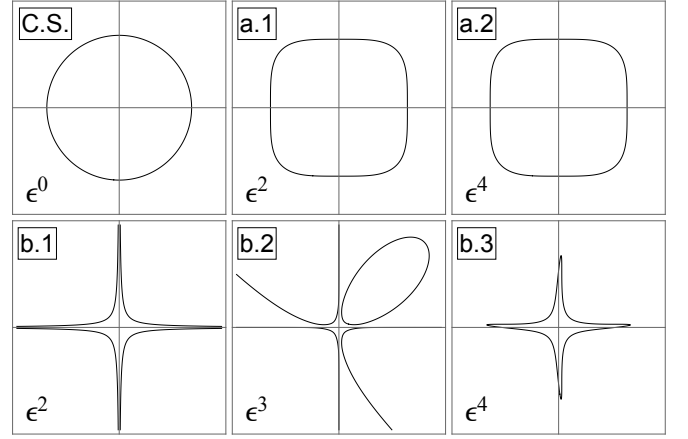


FIG. 9. Invariant curves for small amplitudes $\{\mathcal{K}^{(n)}\}[p, q] \approx 0$ at the $r_4 = 0$ resonance for the zeroth-order linearized approximation (C.S.), cubic (a.) and quadratic (b.) Hénon maps. Cases (a.1-2) and (b.1-3) illustrate the level sets obtained by retaining lower-order terms from the converged expressions in Eqs. (12) and (13), truncated up to ϵ^n , as indicated at the bottom left corner of each plot.

$$\{\mathcal{K}_{b=1}^{(4)}\} = \Pi^2 \epsilon^2 + (\Pi - \text{C.S.}) \Pi \Sigma \epsilon^3 + 2 \Pi^3 \epsilon^4,$$

$$\{\mathcal{K}_{b=1}^{(5)}\} = \Pi^2 \epsilon^2 + (\Pi - \text{C.S.}) \Pi \Sigma \epsilon^3 + \left(2 \Pi^3 - \Pi^2 \text{C.S.} + \frac{\text{C.S.}^3}{3} \right) \epsilon^4 + (\Pi - \text{C.S.}) \Pi^2 \Sigma \epsilon^5, \quad (13)$$

such that $\{\mathcal{K}_{b=1}^{(n \geq 6)}\} = \{\mathcal{K}_{b=1}^{(5)}\} + \mathcal{O}(\epsilon^6)$, and where the expansion must be carried out up to $n = 5$ to obtain converged terms that define a closed level set of the invariant.

Fig. 9, cases (b.1) – (b.3), illustrates the level sets obtained by retaining lower-order terms in Eq. (13). The closer one examines trajectories near the origin, the better the curve (b.3) aligns with numerical tracking results. However, in the infinitesimally small amplitude limit, the dominant term $\Pi^2 \epsilon^2$ alone determines the structure, forming branches of a quadratic hyperbola.

Analyzing the converged terms for a general force function $f(p) = ap + bp^2 + cp^3 + \dots$ at the $1/4$ resonance, we obtain

$$\{\mathcal{K}_{a=0}\} = \left[(b^2 - c) \Pi^2 + c \frac{\text{C.S.}^2}{2} \right] \epsilon^2 + \dots$$

This expression reveals that a stable level set in terms $\propto \epsilon^2$ does not form only when $c = 0$. Moreover, only when $b^2 = c$, does the small-amplitude limit correspond to a circular level set, with the expansion beginning with a C.S.^2 term rather than C.S.. In this case, the higher-order twist coefficients remain finite. Additional details on the higher-order terms that converge for this and other low-order resonances can be found in Appendix A 4.

Fig. 10 compares the results of tracking (top left plot) with averaged non-resonant approximate invariants computed up to order $n = 16$. Unlike Fig. 9, this figure dis-

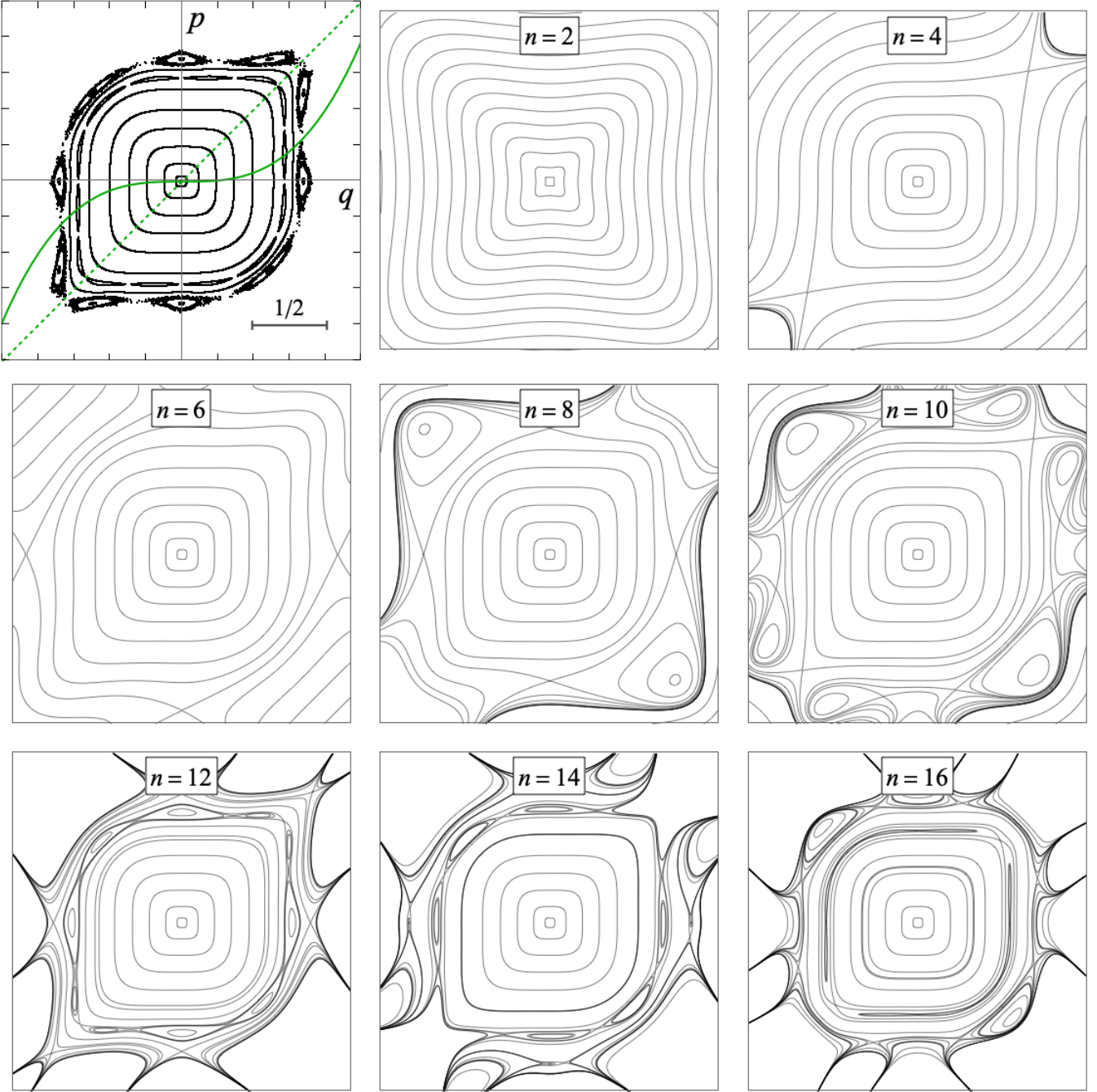


FIG. 10. Trajectories of the Hénon cubic map $f(p) = ap + p^3$ at the $1/4$ integer resonance (top left), compared with approximate non-singular averaged invariants $\{\mathcal{K}_{c=1}^{(n)}\}[p, q]$. The bar scale provides a reference for size, with all approximate invariants displayed on the same grid. Green curves indicate the first (dashed) and second (solid) symmetry lines.

plays the complete invariant at each order, rather than only the converged terms. As n increases, the approximate invariant progressively reveals finer details of the dominant 10-island structure surrounding the central stability region. By $n = 12$, all 10 islands become visible. However, at higher orders, perturbation theory shifts focus to the next 14-island chain nested within the 10-

island structure. At $n = 16$, magnification reveals 10 out of the 14 islands along with associated saddles. As a consequence of this infinite sequence of shifts to finer chains of islands with higher periods, the terms associated with these resonances fail to converge.

Fig. 11, similar to 10, presents averaged non-resonant invariants for quadratic map $f(p) = p^2$. While the largest

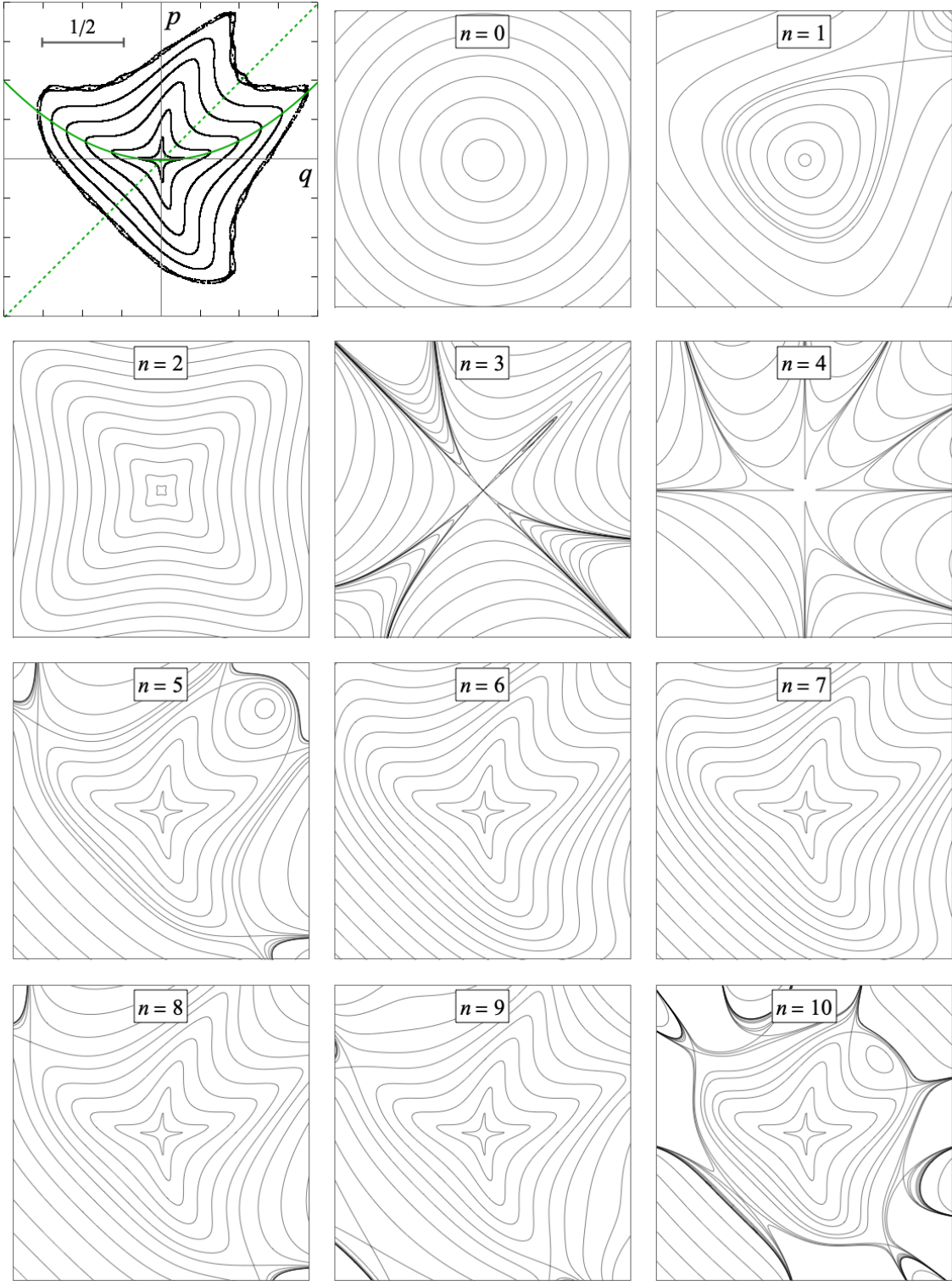


FIG. 11. Same as Fig. 10, but for the quadratic map $f = ap + p^2$ at the quarter-integer resonance ($a = 0$).

visible chain on this scale consists of 21 islands, we do not expect lower-order perturbation theory to capture its full structure. However, for $n = 5$ and $n \geq 8$, the simply connected region surrounding the origin provides a reason-

able approximation of the stable trajectories observed in numerical simulation. In the final section, we explore this question in greater detail, extending our analysis beyond the resonant case to the more general scenario.

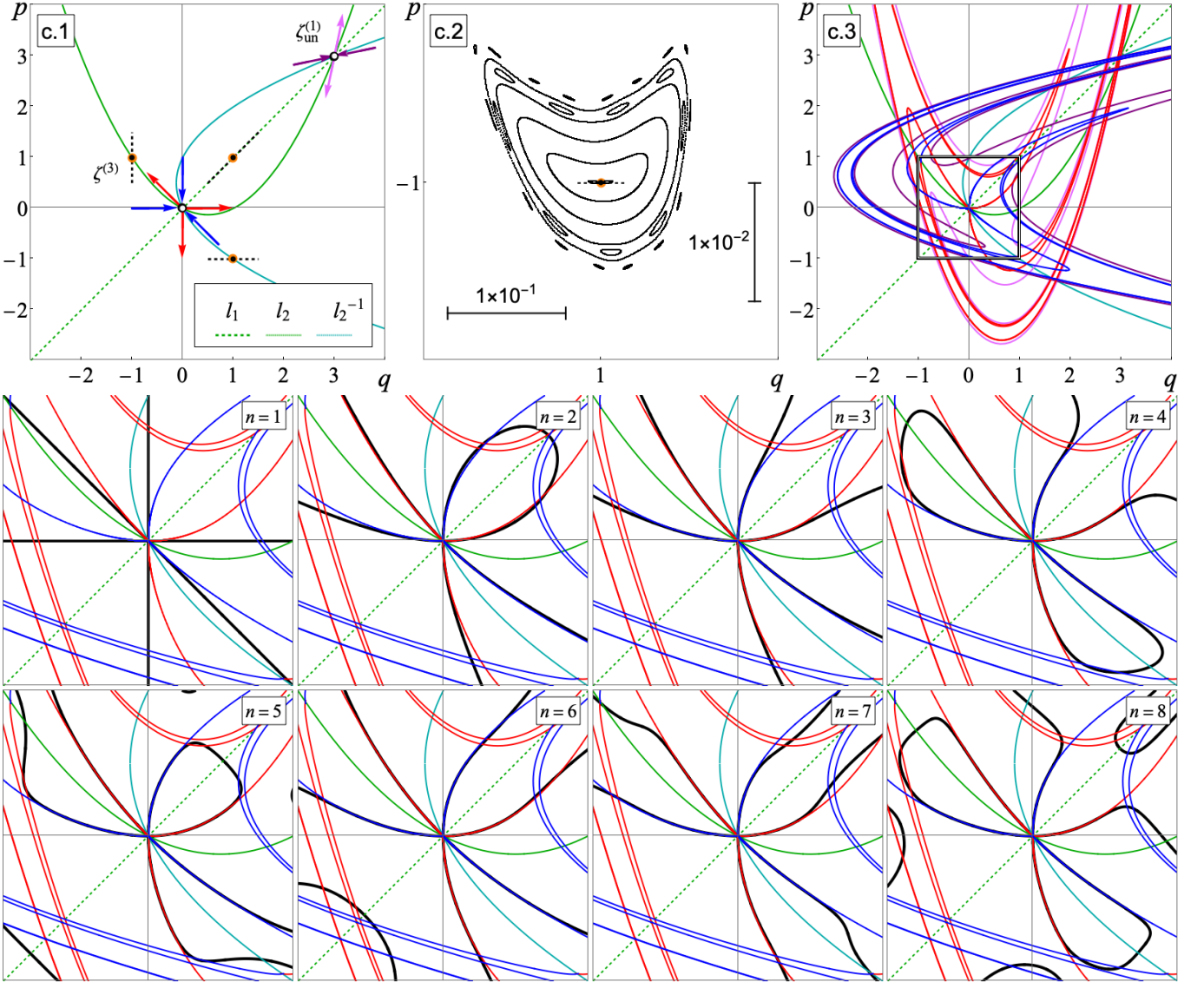


FIG. 12. The top row illustrates some key invariant structures for the Hénon quadratic map at the third-integer resonance $\nu_0 = 1/3$ ($a = 0$). Plot (c.1) highlights unstable fixed point $\zeta_{\text{un}}^{(1)}$, the fixed point at the origin that undergoes a touch-and-go bifurcation with an unstable 3-cycle, and the neutral 3-cycle $\zeta^{(3)}$, which is on the verge of a period-doubling bifurcation. Linearized eigenvectors associated with stable (blue and purple) and unstable (red and pink) manifolds are shown, while the dashed black line indicates the direction of the eigenvector for points with neutral stability. Plot (c.2) provides a magnified view of one of the points in the parabolic 3-cycle $\zeta^{(3)}$, revealing some of the surviving KAM circles. Since the 3-cycle undergoes a period-doubling bifurcation, the horizontal-to-vertical aspect ratio is set to 1:10 for better visibility. Plot (c.3), shown on the same scale as (c.1), presents the stable and unstable manifolds associated with both fixed points, with a black rectangle marking the area for further comparison. The two bottom rows display the zero-level set of the approximate non-singular averaged invariant $\{\mathcal{K}_{a,b=1}^{(n)}\}[p, q] = 0$ alongside the actual continuations of the stable and unstable manifolds from (c.3). Green curves represent the first (dashed) and second (solid) symmetry lines, while the cyan curve corresponds to the inverse of the second symmetry, l_2^{-1} .

2. Third integer resonance, $\nu_0 = 1/3$

Another important example is the system at the third-integer resonance, $\nu_0 = 1/3$ ($a = -1$). For a general force function with $b \neq 0$, even the first twist coefficient τ_0 becomes singular, resulting in unstable motion near the origin. The bottom row (c.) of Fig. 8 illustrates the phase

space transformation for the simple quadratic Hénon map $f(p) = ap + p^2$. When the system is slightly detuned from the resonance, $\delta_r = \nu_r - \nu_0 \neq 0$, the invariant curves of small-amplitude oscillations near the origin resemble ellipses described by:

$$\text{C.S.}[a = -1] = p^2 + pq + q^2. \quad (14)$$

However, at the exact resonance, $\delta_r = 0$, the unstable 3-cycle, which otherwise defines the distinct triangular shape, undergoes a touch-and-go bifurcation with the fixed point at the origin. Although the system exhibits local instability, some invariant features persist, as highlighted in Fig. 12. In plot (c.1), the system's fixed points and 3-cycles are displayed along with the corresponding eigenvectors, obtained by linearizing the Jacobian at each periodic orbit. Plot (c.2) zooms into the region around the second 3-cycle $\zeta^{(3)}$ (orange) at the point $(1, -1)$, showing some of the surviving KAM circles. Since $\zeta^{(3)}$ undergoes a period-doubling bifurcation, giving rise to a 6-cycle when $\nu_0 > \nu_r$, it has neutral stability with only one eigenvector, represented by the dashed black line. Plot (c.3) further illustrates the extension of the eigenvectors along the stable (blue and purple) and unstable (red and pink) manifolds, originating from both the fixed point at the origin and the unstable fixed point $\zeta_{\text{un}}^{(1)}$. As expected in chaotic systems, the manifolds exhibit homo- and heteroclinic intersections, forming a complex web-like structure often referred to as a *tangle* [44].

Since the perturbation expansion is constructed around the fixed point at the origin, the associated stable and unstable manifolds serve as exact invariant structures that the theory should ideally capture. While perturbation theory is not expected to accurately describe regions dominated by tangles, it can still provide reliable approximations in the vicinity of the origin where the structure remains relatively simple (highlighted by the black square). The subsequent two rows in Fig. 12 present the zero-level set of the approximate non-singular averaged invariant:

$$\{\mathcal{K}_{b=1}^{(n)}\}[p, q] = 0$$

compared to the actual extensions of the stable and unstable manifolds from plot (c.3). While the stable and unstable manifolds attached to the fixed point are each invariant in the sense of Eq. (3), their union forms a symmetric set that remains invariant under Eqs. (4) and (5). As anticipated, within the chosen region, the zero-level set at each successive order provides an increasingly accurate approximation of the union of the manifolds. The expansion effectively serves as a power series representation, progressively refining the depiction of the invariant structure.

To gain a clearer understanding of the behavior near the origin when $\delta_r = 0$, we examine the analytical expressions obtained at the first few orders:

$$\begin{aligned} \{\mathcal{K}_{b=1}^{(1)}\} &= -\Pi \Sigma \epsilon, \\ \{\mathcal{K}_{b=1}^{(2)}\} &= -\Pi \Sigma \epsilon - \left(\Pi^2 - \frac{5}{6} \frac{\text{C.S.}^2}{2} \right) \epsilon^2, \\ \{\mathcal{K}_{b=1}^{(3)}\} &= -\Pi \Sigma \epsilon - \left(\Pi^2 - \frac{\text{C.S.}^2}{2} \right) \epsilon^2 - \\ &\quad - \left(\Pi + \frac{7}{9} \frac{\text{C.S.}}{2} \right) \Pi \Sigma \epsilon^3, \end{aligned}$$

$$\begin{aligned} \{\mathcal{K}_{b=1}^{(n \geq 4)}\} &= -\Pi \Sigma \epsilon - \left(\Pi^2 - \frac{\text{C.S.}^2}{2} \right) \epsilon^2 - \\ &\quad - \left(\Pi - \frac{\text{C.S.}}{2} \right) \Pi \Sigma \epsilon^3 + \mathcal{O}(\epsilon^4). \end{aligned}$$

The terms in $\mathcal{K}_{b=1}^{(n \geq 4)}$ converge up to ϵ^3 , which accounts for the local instability near the origin. The dominant first-order term, proportional to $\Pi \Sigma$, represents the linearized contribution to the invariant.

Next, considering the case of a general smooth force function given by $f(p) = ap + bp^2 + cp^3 + dp^4 + \dots$. The approximate invariant becomes

$$\{\mathcal{K}_{a=-1}\} = -b \Pi \Sigma \epsilon - \left[b^2 \Pi^2 - (b^2 + c) \frac{\text{C.S.}^2}{2} \right] \epsilon^2 + \mathcal{O}(\epsilon^3),$$

as detailed in Appendix A 4. Notably, for small amplitudes, the invariant curves coincide with ellipses described by Eq. (14) only if $b = 0$ and $c \neq 0$; in this scenario, the expansion begins with a C.S.² term, similar to the previously considered $\nu_0 = 1/4$ case. However, when both $b, c = 0$ and $d \neq 0$, the system becomes unstable once again, with the leading-order behavior described by:

$$\{\mathcal{K}_{a=-1; b, c=0}\} = -d \Pi \Sigma \text{C.S.} \epsilon^3 + \mathcal{O}(\epsilon^4),$$

consistent with the phenomenon of decapole instability in accelerator physics [19].

E. Action-angle variables

Having constructed the approximate invariant and developed the averaging procedure, we now turn our attention to how these results can be connected to other perturbation theories, including Lie algebra methods and related approaches. In particular, we address the key question of how to derive the approximate action-angle variables Eq. (10)

$$J' = J,$$

$$\theta' = \theta + 2\pi \nu(J),$$

and how to obtain the twist coefficients or even the full expression for the rotation number $\nu(J)$ when the series converges:

$$\nu(J) = \nu_0 + \tau_0 J + \frac{1}{2!} \tau_1 J^2 + \frac{1}{3!} \tau_2 J^3 + \dots \quad (15)$$

This naturally leads us to the fundamental question: “Given an invariant of motion and the mapping equations, how can one determine the rotation number for a system that is exactly integrable?” To our knowledge, this question was first articulated by Slava Danilov during his Ph.D. studies at the Budker Institute of Nuclear Physics, under the supervision of E. Perevedentsev. His insights were initially published and generalized in [58, 59], and later extended to higher dimensions in [60, 61].

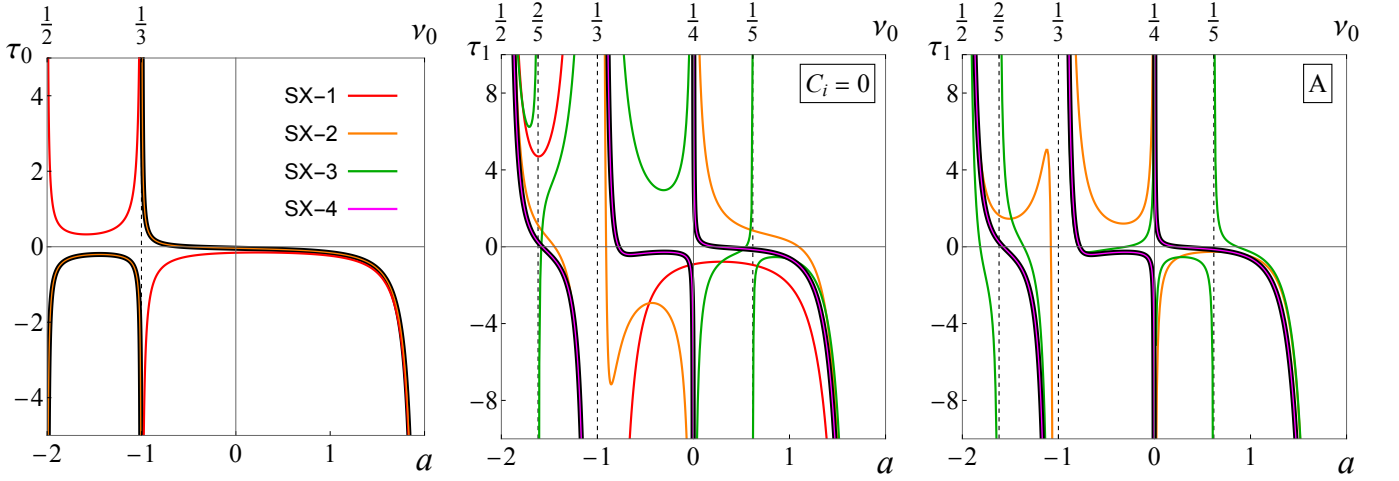


FIG. 13. First two twist coefficients, $\tau_0(a)$ and $\tau_1(a)$, as functions of the trace for the Hénon quadratic map $f(p) = ap + p^2$. The thick black curves represent results obtained using the Lie algebra method, Eqs. (11) and (A2,A3). Colored curves correspond to twist coefficients derived from the approximate invariants $\mathcal{K}_{b=1}^{(n)}[p, q]$ and are labeled SX- n as indicated in the legend. Two sets of plots for τ_1 are obtained: one using non-averaged invariants $\mathcal{K}_{b=1}^{(n)}[p, q]$ with all C_i set to zero, and another using the averaged invariants $\{\mathcal{K}_{b=1}^{(n)}\}[p, q]$, (A). Convergence is observed for τ_0 at $n \geq 2$ and for τ_1 at $n \geq 4$, irrespective of averaging. The complementary scale at the top indicates the bare rotation number, highlighting the relevant resonances.

Theorem 1 (Slava Danilov) Consider a symplectic map of the plane $\mathbb{T} : \zeta \mapsto \zeta'$, which is integrable with an invariant (integral of motion) $\mathcal{K}[p, q]$ such that:

$$\forall \zeta = (p, q) \in \mathbb{R}^2 : \quad \mathcal{K}[\zeta'] - \mathcal{K}[\zeta] = 0.$$

Then, the Poincaré rotation number on a closed level set $\mathcal{K}[p, q] = \text{const}$, surrounding the fixed point, is given by the ratio:

$$\nu(\mathcal{K}) = \int_{\zeta_0}^{\zeta_0'} \left(\frac{\partial \mathcal{K}}{\partial p} \right)^{-1} dq / \oint_{\mathcal{K}=\text{const}} \left(\frac{\partial \mathcal{K}}{\partial p} \right)^{-1} dq.$$

Alternatively, it can be expressed as:

$$\nu(\mathcal{K}) = \frac{dJ'(\mathcal{K})}{dJ(\mathcal{K})}.$$

Here, J and J' represent the action and partial action, respectively, defined as:

$$J(\mathcal{K}) = \oint_{\mathcal{K}=\text{const}} \frac{p dq}{2\pi}, \quad J'(\mathcal{K}) = \int_{\zeta_0}^{\zeta_0'} \frac{p dq}{2\pi}.$$

In all cases, the integrals are taken along the invariant curve $\mathcal{K}[p, q] = \text{const}$. $\int_{\zeta_0}^{\zeta_0'}$ refers to an integral over one iteration of the map, remaining unaffected by the choice of initial point $\zeta_0 = (p_0, q_0)$, whereas \oint indicates a contour integral encompassing the entire closed curve.

Therefore, at each order of the perturbation theory, within the simply connected region around the fixed point, we can define an approximate action and rotation

number associated with the invariant $\mathcal{K}^{(n)}[p, q]$:

$$J^{(n)}(\mathcal{K}^{(n)}) \equiv J(\mathcal{K}^{(n)}) = \oint_{\mathcal{K}^{(n)}=\text{const}} \frac{p dq}{2\pi},$$

$$\nu^{(n)}(\mathcal{K}^{(n)}) = \frac{dJ'(\mathcal{K}^{(n)})}{dJ(\mathcal{K}^{(n)})}.$$

By expanding both quantities in a power series of $\mathcal{K}^{(n)}$, we obtain the desired expansion:

$$\nu^{(n)}(J) = \nu_0 + \tau_0^{(n)} J + \frac{1}{2!} \tau_1^{(n)} J^2 + \frac{1}{3!} \tau_2^{(n)} J^3 + \dots$$

Comparing this expansion with the coefficients τ_k derived using the Lie algebra method, we find that at any given order $n \geq 0$ and for any values of C_i , the following general result holds:

$$\tau_k^{(n)} = \tau_k \quad \text{for} \quad -1 \leq k \leq \lfloor n/2 \rfloor - 1,$$

where $\tau_{-1} \equiv \nu_0$. In other words, at each even order $n = 2m$, all coefficients up to $\tau_{m-1}^{(n)}$ converge to their corresponding exact values τ_{m-1} .

Fig. 13 presents a comparison between the exact coefficients τ_k (shown as black thick curves) and the approximate coefficients $\tau_k^{(n)}$ (colored curves) obtained from different orders of PT up to $n = 4$. For illustration, we once again use the quadratic Hénon map, $f(p) = ap + p^2$. The results for the approximate invariants $\mathcal{K}_{b=1}^{(n)}[p, q]$ are labeled as SX- n , representing their application to horizontal dynamics in an accelerator with a thin sextupole (SX) magnet [50]. The leftmost plot shows τ_0 , where the convergence of the second-order approximation is evident, as expected; here recall that SX-1 is independent of all C_i , while without averaging, SX-2 and SX-3 are determined solely by C_1 , and, SX-4 depends on both C_1 and C_2 .

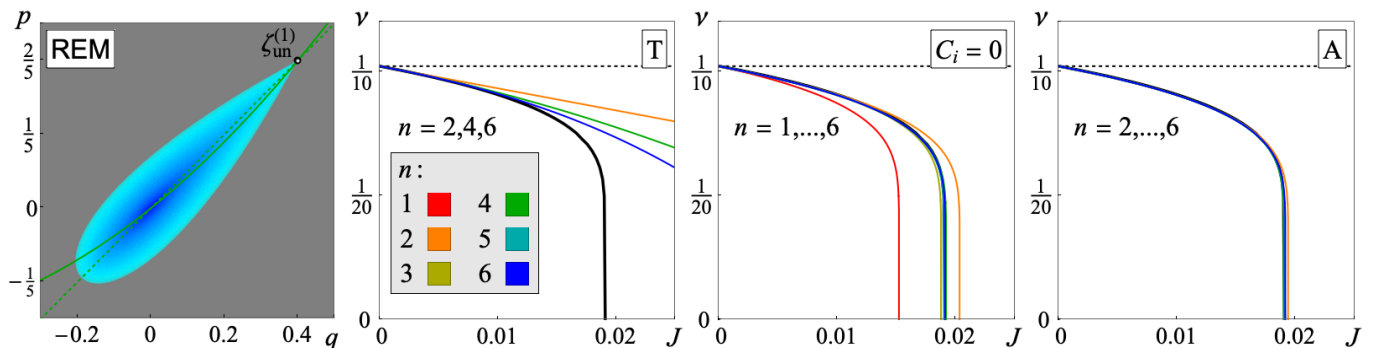


FIG. 14. The left plot displays the phase space of the Hénon quadratic map $f(p) = ap + p^2$, at $a = 8/5$, with colors representing the REM indicator. The three plots on the right compare approximations of $\nu(J)$ (colored curves), obtained using different methods: the Taylor series (T) expansion of $\nu[J = 0] = \nu_0 + \tau_0 J + \dots$ via the Lie algebra method (up to J^3 , i.e., $n = 6$), non-averaged invariants with $C_i = 0$, and the averaged invariants $\langle \mathcal{K}^{(n)} \rangle[p, q]$ (A). The black solid curve represents results obtained from numerical tracking, where J is estimated as the area enclosed by an orbit over 2π .

The fact that the *detuning* τ_0 , as defined in Eq. (11), remains independent of C_1 has notable consequences for maps with *typical* force functions, i.e., $b \neq 0$ or $c \neq 0$. In particular, the second-order approximate invariant takes the form

$$\mathcal{K}^{(2)}[p, q] = \text{C.S.} + \beta \Pi \Sigma \epsilon + (\alpha \Pi^2 + C_1 \text{C.S.}^2) \epsilon^2,$$

where

$$\alpha = \frac{b^2}{r_3 r_4} - \frac{c}{r_4}, \quad \text{and} \quad \beta = -\frac{b}{r_3}. \quad (16)$$

Eq. (16) establishes a direct correspondence between a typical map and an integrable McMillan map characterized by the symmetric invariant $\mathcal{K}^{(2)}[p, q]$ with $C_1 = 0$, and the force

$$f_1(p) = -\frac{\beta p^2 - ap}{\alpha p^2 + \beta p + 1} = ap + bp + cp^2 + \mathcal{O}(p^3).$$

This correspondence guarantees that the force functions are identical up to $\mathcal{O}(\epsilon^3)$, which, in turn, ensures that the rotation number expansions around the fixed point also match up to the leading nonlinear term, $\nu = \nu_0 + \tau_0 J$. As shown in [50, 51], integrable McMillan maps offer a robust framework for understanding the behavior of typical mappings near the main resonances, particularly $1/4$ and $1/3$, as well as integer and half-integer resonances. The analytical expressions and series expansions in these references offer the necessary foundation to describe the lower orders of PT.

The two final plots in Fig. 13 illustrate the behavior of the next twist coefficient τ_1 . The middle plot shows the values of the second detuning with all C_i set to zero, while the last plot (labeled “A”) presents results obtained using the averaging procedure. In both cases, the twist coefficient from the fourth-order invariant (SX-4, magenta curve) aligns perfectly with the prediction from the Lie algebra method (black curve). While convergence is not expected for $n = 2, 3$ (orange and green curves), careful inspection reveals that averaging improves the results,

particularly near main resonances like the integer value $\nu_0 = 0$ and $1/2, 1/3, 1/4$.

At this point, we have established that the converged terms of the $\nu(J)$ series at $J = 0$ yield the same results across different methods — whether derived from the Lie algebra approach, perturbation theory (averaged or not), or direct numerical experiments. This naturally leads to the next important questions: “Can $\nu^{(n)}(J)$ obtained from PT offer advantages over the traditional expansion?” and “How does the choice of C_i influence the results?” While we explore the benefits of the averaging procedure in the following sections, here we highlight one particularly notable example.

Consider the quadratic Hénon map slightly detuned from an integer resonance, with $\nu_0 - \nu_r \approx 0.1$. This case provides an example of *quasi-integrable* dynamics, where the stable region is largely dictated by the invariant manifolds associated with the second unstable fixed point, $\zeta_{un}^{(1)}$. It not only has a relatively well-defined stability boundary but also lacks visible island chains (though they do appear at smaller scales), as seen in Fig 14. The left plot shows the phase space using the REM [64–66] indicator applied to a dense set of initial conditions. Since our focus here is on enhancing the visualization compared to previously used individual orbits, we omit the color scale but note that more regular orbits appear in shades of blue to cyan, while chaotic ones are marked in red and black (see also Figures in the second part of this manuscript).

Besides a direct comparison of analytical approaches, quasi-integrability allows for the extraction of both the action (as the area enclosed by iterates of an orbit) and the rotation number from numerical experiments (black curve in all three plots). For a detailed discussion of the numerical method used, refer to Section 6.1.2 of [50]. A direct comparison of the curves reveals two key observations: (i) PT provides a significantly more accurate approximation of numerically computed $\nu(J)$ compared to the Taylor series (T), and (ii) averaging (A) further improves accuracy. This is evident, for example, when comparing the orange curves in the last two plots.

III. POSSIBLE GENERALIZATIONS

A. Symmetries

A natural question for the curious reader is: what makes the first symmetry special compared to the second, given that it is exactly satisfied at every order? This question becomes especially intriguing when one considers the inverse mapping T^{-1} , which reverses the symmetry ordering.

To explore this, we extend our analysis to a more general class of maps [18], related to the integrable asymmetric McMillan map [53] and the QRT family [67, 68]. Consider a composite mapping constructed from two McMillan-form transformations (2), each with a different force function [18, 53]:

$$\begin{aligned} T_a : q' &= -q + f_1(p), \\ p' &= -p + f_2(q'). \end{aligned} \quad (17)$$

This map is again reversible and symplectic for arbitrary force functions $f_{1,2}$, and can be expressed as a composition of two anti-area-preserving involutions, i.e., $T_a = R_2^{(a)} \circ R_1^{(a)}$:

$$\begin{aligned} R_1^{(a)} : q' &= -q + f_1(p), & R_2^{(a)} : q' &= q, \\ p' &= p, & p' &= -p + f_2(q). \end{aligned}$$

The corresponding symmetry lines are:

$$l_1^{(a)} : q = f_1(p)/2 \quad \text{and} \quad l_2^{(a)} : p = f_2(q)/2,$$

where now both $l_1^{(a)}$ and $l_2^{(a)}$ are defined by general functions.

We proceed with a perturbative expansion, starting again from a general polynomial substitution. Assuming a fixed point at the origin, $f_{1,2}(0) = 0$, the zeroth-order approximation yields the linearized invariant (up to an overall factor C_0)

$$\mathcal{K}_0^{(a)}[p, q] = a_1 p^2 - a_1 a_2 p q + a_2 q^2,$$

with the associated bare rotation number

$$\nu_0 = \frac{1}{2\pi} \arccos \frac{\sigma}{2}, \quad \sigma = a_1 a_2 - 2,$$

where σ is the trace of the Jacobian matrix evaluated at the origin.

Before moving to higher orders, recall that for the symmetric map, the approximate invariant $\mathcal{K}^{(n)}[p, q]$ had two distinct contributions. The first was a power series of the zeroth-order invariant

$$C_0 \text{C.S.} + C_1 \text{C.S.}^2 + C_2 \text{C.S.}^3 + \dots,$$

defined up to an overall multiplier C_0 (seed), with higher-order coefficients determined via the averaging procedure. In contrast, the second set of terms contributes

independently and can be determined directly from the approximate invariance condition. These terms can be expressed in a matrix form:

$$\begin{bmatrix} 1 \\ q \\ q^2 \\ q^3 \\ q^4 \\ q^5 \\ \vdots \end{bmatrix} \cdot \begin{bmatrix} 0 & 0 & \ominus & \oplus & \ominus & \oplus & \ominus \\ 0 & \ominus & C_{2,1} & \ominus & C_{4,1} & \ominus & \\ \ominus & C_{1,2} & C_{2,2} & C_{3,2} & C_{4,2} & & \\ \oplus & \ominus & C_{2,3} & C_{3,3} & & & \\ \ominus & C_{1,4} & C_{2,4} & & & & \\ \oplus & \ominus & & & & & \\ \ominus & & & & & & \end{bmatrix} \begin{bmatrix} 1 \\ p \\ p^2 \\ p^3 \\ p^4 \\ p^5 \\ \vdots \end{bmatrix}.$$

Here, per Proposition 1, the coefficients satisfy the symmetry $C_{i,j} = C_{j,i}$. Additional Propositions 2 – 3, dictate that terms proportional to p^{2k+1} and q^{2k+1} vanish (marked \oplus), while specific even-order terms p^{2k} , $p^{2k-1}q$, pq^{2k-1} , q^{2k} (marked \ominus) are constrained and can be set to zero to match the integrable symmetric McMillan mapping for $C_{i>0} = 0$.

In the asymmetric case, the symmetry $C_{i,j} = C_{j,i}$ is lost. Nonetheless, the structure of the approximate invariant still follows the form

$$C_0 \mathcal{K}_0 + C_1 \mathcal{K}_0^2 + C_2 \mathcal{K}_0^3 + \dots$$

plus additional matrix, which now has less symmetry

$$\begin{bmatrix} 1 \\ q \\ q^2 \\ q^3 \\ q^4 \\ q^5 \\ \vdots \end{bmatrix} \cdot \begin{bmatrix} 0 & 0 & \ominus & \oplus & \ominus & \oplus & \ominus \\ 0 & \ominus & C_{2,1} & \ominus & C_{4,1} & \ominus & \\ \ominus & C_{1,2} & C_{2,2} & C_{3,2} & C_{4,2} & & \\ \oplus & C_{1,3} & C_{2,3} & C_{3,3} & & & \\ C_{0,4} & C_{1,4} & C_{2,4} & & & & \\ \oplus & C_{1,5} & & & & & \\ C_{0,6} & & & & & & \end{bmatrix} \begin{bmatrix} 1 \\ p \\ p^2 \\ p^3 \\ p^4 \\ p^5 \\ \vdots \end{bmatrix}.$$

Odd terms p^{2k+1} and q^{2k+1} again vanish. For the even-order terms, only one of the two pairings can be simultaneously eliminated: either the pair p^{2k} and $p^{2k-1}q$ (marked with \ominus), or the pair pq^{2k-1} and q^{2k} . Choosing the former set aligns the mapping with an asymmetric McMillan map, characterized by the following force functions:

$$f_1(p) = -\frac{\delta p^2 + \varepsilon p}{\alpha p^2 + \beta p + \gamma}, \quad f_2(q) = -\frac{\beta q^2 + \varepsilon q}{\alpha q^2 + \delta q + \kappa},$$

with biquadratic invariant

$$\mathcal{K}[p, q] = \alpha p^2 q^2 + \beta p q^2 + \delta p^2 q + \gamma q^2 + \varepsilon p q + \kappa p^2,$$

and matched twist coefficient τ_0 when $C_1 = 0$. The coefficients (and the invariant itself) are defined up to a common factor, let say ε , with relations:

$$\begin{aligned} \beta &= \frac{\varepsilon}{a_1 a_2} \frac{a_2^2 b_1 - a_1 b_2}{a_1 a_2 - 1}, & \gamma &= -\frac{\varepsilon}{a_1}, \\ \delta &= \frac{\varepsilon}{a_1 a_2} \frac{a_1^2 b_2 - a_2 b_1}{a_1 a_2 - 1}, & \kappa &= -\frac{\varepsilon}{a_2}, \end{aligned}$$

and

$$\begin{aligned}\alpha &= \frac{\varepsilon}{a_1^2 a_2} \left(a_2 c_1 - \frac{a_2^2 b_1 - a_1 b_2}{a_1 a_2 - 1} b_1 \right) \\ &= \frac{\varepsilon}{a_1 a_2^2} \left(a_1 c_2 - \frac{a_1^2 b_2 - a_2 b_1}{a_1 a_2 - 1} b_2 \right).\end{aligned}$$

Proceeding to the evaluation of the two-indexed coefficients $C_{i,j}$, the next-order contributions to the approximate invariant take the form:

$$\begin{aligned}\mathcal{K}_1^{(a)}[p, q] &= -\frac{pq}{R_3} [(a_1^2 b_2 - a_2 b_1) p + (a_2^2 b_1 - a_1 b_2) q], \\ \mathcal{K}_2^{(a)}[p, q] &= \frac{p^2 q^2}{R_3 R_4} \left[L_{2,2} + L_{0,4} \left(1 - \frac{q}{a_1 p} \right)^2 \right], \\ \dots\end{aligned}$$

where

$$\begin{aligned}L_{2,2} &= \frac{b_1(a_2^2 b_1 - a_1 b_2) - a_2 c_1 R_3}{a_1} R_4, \\ L_{0,4} &= a_1^3 b_2^2 - a_2^3 b_1^2 + (a_2^2 c_1 - a_1^2 c_2) R_3,\end{aligned}$$

and the resonant denominators that can be expressed in terms of their symmetric counterparts as $R_k = r_k [a = \sigma]$. For instance,

$$R_3 = a_1 a_2 - 1, \quad R_4 = a_1 a_2 - 2.$$

Analyzing these polynomials, we find that — except in the integrable asymmetric McMillan map case — none of the symmetries are exactly preserved at finite order. Instead, $\mathcal{K}^{(n)}[p, q]$ respects both symmetries to an accuracy matching the order, as given by Eq. (6). The linear part of the symmetries is recovered in zeroth order, the quadratic in first order, and so on. This explains why the linear symmetry line $l_1: p = q$ (for the symmetric map T) appears to be favored as one proceeds to higher orders.

B. Form of the map

The same technique can be applied to a general symplectic map that admits a polynomial representation:

$$\begin{aligned}q' &= A_{1,0} q + A_{0,1} p + A_{2,0} q^2 + A_{1,1} qp + A_{0,2} p^2 + \dots, \\ p' &= B_{1,0} q + B_{0,1} p + B_{2,0} q^2 + B_{1,1} qp + B_{0,2} p^2 + \dots\end{aligned}$$

We briefly summarize the general procedure here.

- We begin by introducing a general polynomial ansatz for the approximate invariant, where each \mathcal{K}_m is a homogeneous polynomial of degree $m + 2$:

$$\mathcal{K}^{(n)}[p, q] = \mathcal{K}_0 + \varepsilon \mathcal{K}_1 + \dots + \varepsilon^n \mathcal{K}_n,$$

which we require to be conserved up to order $\mathcal{O}(\varepsilon^{n+1})$

$$\mathcal{R}_n = \mathcal{K}^{(n)}[p', q'] - \mathcal{K}^{(n)}[p, q] = \overline{\mathcal{R}_n} \varepsilon^{n+1} + \mathcal{O}(\varepsilon^{n+2}).$$

The lowest-order terms of the approximate invariant — also obtainable through standard linearization — are defined up to a common multiplicative factor

$$\mathcal{K}_0[p, q] = C_0 [A_{0,1} p^2 + (A_{1,0} - B_{0,1}) pq - B_{1,0} q^2].$$

The seed coefficient C_0 can be set to unity, or to a specific value chosen to eliminate resonant denominators. Alternatively, choosing $C_0 = \beta^*/A_{0,1}$, where β^* is the beta-function at a given location in an accelerator, recovers the conventional Courant-Snyder invariant, $C_0 \mathcal{K}_0 = \text{em}$, where em is the beam emittance, defining the area occupied by the beam in phase space.

- Due to under-determinacy, the invariant (after all two-indexed coefficients $C_{i,j}$ have been determined) is known only up to a series

$$C_0 \mathcal{K}_0 + C_1 \mathcal{K}_0^2 + \dots$$

Nevertheless, the approximate invariance condition holds to the required order, and the twist coefficient τ_k converges at order $n = 2k + 2$.

- To determine the coefficients C_i (for $i > 0$), we use an averaging procedure. Using the eigenbasis of the Jacobian $(q, p) \rightarrow (Q, P)$, the linear part of the map is transformed into a pure rotation:

$$\begin{aligned}Q' &= Q \cos(2\pi\nu_0) - P \sin(2\pi\nu_0) + \dots, \\ P' &= Q \sin(2\pi\nu_0) + P \cos(2\pi\nu_0) + \dots,\end{aligned}$$

and the linearized invariant becomes:

$$\mathcal{K}_0[P, Q] = P^2 + Q^2.$$

In accelerator physics, this transformation is typically achieved through the use of Floquet variables. Switching to polar coordinates:

$$Q = \rho \cos \psi, \quad P = \rho \sin \psi,$$

the coefficients C_k are determined by solving the system:

$$\frac{d}{dC_k} I_n = 0,$$

which minimizes the integral

$$I_n = \int_0^{2\pi} \overline{\mathcal{R}_n}^2[\rho, \psi] d\psi.$$

- **Note:** If the map is not explicitly constructed from a sequence of symplectic transformations, one must ensure symplecticity by enforcing conditions such as:

$$\begin{aligned}A_{1,0} B_{0,1} - B_{1,0} A_{0,1} &= 1, \\ A_{1,1} B_{0,1} + 2 A_{1,0} B_{0,2} - 2 A_{0,2} B_{1,0} - A_{0,1} B_{1,1} &= 0, \\ A_{1,1} B_{1,0} + 2 A_{0,1} B_{2,0} - 2 A_{2,0} B_{0,1} - A_{1,0} B_{1,1} &= 0, \\ \dots\end{aligned}$$

C. Dimensions

Finally, we note that this approach can be extended to systems of higher dimensionality. For instance, in a 4D symplectic map involving two coordinates and momenta (x, p_x, y, p_y) , and assuming linearly decoupled dynamics, one begins with horizontal and vertical quadratic invariants: “horizontal” $\mathcal{K}_0^{(x)}[x, p_x]$ and “vertical” $\mathcal{K}_0^{(y)}[y, p_y]$. Nonlinear coupling is then recovered in higher-order terms such as $\mathcal{K}_1^{(x,y)}[x, p_x, y, p_y]$. In this case, trajectories are no longer confined to a single level set, but instead lie on the intersection of two 4D hypersurfaces. This complicates the analysis but still allows for accurate estimates. We leave a detailed discussion to a separate article.

IV. CONCLUSIONS AND DISCUSSION

In closing, we would like to comment on the remarkable robustness of particle accelerators to generic perturbations in their nonlinear optics, and the resulting stability this imparts.

Accelerator lattices are often considered “poorly” optimized when it comes to nonlinear elements. This characterization stems from multiple sources. Operationally, not all nonlinear magnets are always available due to technical issues or failures. As accelerator complexes grow older and more expansive, such limitations tend to accumulate. Compounding this, there are numerous sources of parasitic nonlinear fields, arising from fringe effects, magnet imperfections, or design flaws. At best, these imperfections are carefully measured after construction and partially corrected. Nevertheless, the cumulative impact is rarely negligible. And yet, these machines continue to deliver beams reliably, extracting maximum performance from limited resources.

The term *stability* deserves clarification. On one hand, particles in accelerators do exhibit instabilities — often due to collective effects. As beam intensity increases, so too does the influence of interactions among particles and with the environment. Energy growth, likewise, leads to intra-beam scattering.

On the other hand, at lower beam intensities and energies — where collective effects are suppressed and nonlinear magnetic fields dominate — the dynamics of single particles become the primary concern. In this regime, the region of stability is typically defined either by a singular resonance (with clear stable and unstable manifolds, as seen in Fig. 14), or by the overlap of multiple resonances, which results in island chains and chaotic trajectories.

This distinction becomes evident when examining maps in an extended parameter space. In the second part of this article, we use isochronous stability diagrams, where singular resonances yield well-defined boundaries, in contrast to the “ripped” fractal edges created by overlapping resonances (see also [19] for a detailed discussion).

A central question then arises: how can one estimate the region of stability? For singular resonances, the stability region is, roughly speaking, bounded by the distance to the associated unstable fixed point or n -cycle. However, far from any singular resonance (in the space of parameters), estimating the stability region becomes highly nontrivial. What is particularly striking is that resonance overlap tends to occur only at relatively large amplitudes. This allows for a surprisingly large domain of quasi-integrable motion to persist — and, in some cases, even quasi-linear behavior — where chaos indicators such as SALI/GALI or REM vary very little. Similar effects have been observed in piecewise linear systems [41, 42].

We suggest that this persistence of stability (complementing general results from KAM theory) can, at least in part, be understood through the presence of a low-order, nonlinear, integrable map hidden near the origin. This is akin to how symmetric and asymmetric mappings approximate transformations of the corresponding form. Even for a general map, the existence of two symmetry lines intersecting at the fixed point (even if not known explicitly) supports the construction of approximate invariants.

In higher-dimensional systems, such as particle accelerators governed by 6D symplectic maps derived from time-dependent Hamiltonians, the planar approximation can provide remarkably accurate and practical results. In practice, many particle beams are *flat*, meaning their horizontal size is much larger than the vertical, $\sigma_x \gg \sigma_y$. In such settings, horizontal invariants provide highly accurate estimates of dynamic aperture limits imposed by singular resonances. Another notable example is resonant extraction, which exploits a singular resonance to channel streams of particles out of the machine. In this context, approximate invariants once again provide fast and effective estimates — similar to the classical isolated resonance approach.

The third part of this manuscript contains a variety of examples based on general symplectic mappings derived from realistic accelerator lattices across the FermiLab complex, demonstrating the method’s practical efficiency in real-world applications.

V. ACKNOWLEDGMENTS

The authors would like to thank Taylor Nchako (Northwestern University) for carefully reading this manuscript and for her helpful comments. S.N. work is supported by the U.S. Department of Energy, Office of Science, Office of Nuclear Physics under contract DE-AC05-06OR23177. I.M. acknowledges that his work was partially supported by the Ministry of Science and Higher Education of the Russian Federation (project FWUR-2025-0004). S.K. is grateful to his supervisor, Prof. Young-Kee Kim (University of Chicago), for her valuable mentorship and continuous support.

Appendix A: Map in McMillan form with analytic force function

In this appendix, we summarize some analytical results for the map in McMillan form (2), assuming a force function that admits a Taylor series expansion:

$$f(\epsilon p)/\epsilon = ap + \epsilon bp^2 + \epsilon^2 cp^3 + \epsilon^3 dp^4 + \epsilon^4 ep^5 + \epsilon^5 fp^6 + \epsilon^6 gp^7 + \dots, \quad (\text{A1})$$

where $f(0) = 0$, ensuring a fixed point at the origin.

1. Twist expansion

Expanding the rotation number in terms of the action variable up to the third order in J^3 (corresponding to ϵ^6)

$$\nu[J=0] = \nu_0 + \tau_0 J + \frac{1}{2!} \tau_1 J^2 + \frac{1}{3!} \tau_2 J^3 + \dots,$$

for the force function in Eq. (A1), the twist coefficients are given by:

$$\begin{aligned} \frac{2\pi\nu_0}{0!} &= \arccos[a/2], & \frac{2\pi\tau_0}{1!} &= \frac{3}{r_1 r_2} \left[c - \frac{2}{3} \frac{1+2a}{r_1 r_3} b^2 \right], \\ \frac{2\pi\tau_1}{2!} &= \frac{3}{(-r_1 r_2)^{5/2} r_4} \left[\left(1 - \frac{9}{2} a^2\right) c^2 + 4 \frac{t_{11}}{r_1 r_3^2} b^2 c - \frac{2}{3} \frac{t_{12}}{r_1^2 r_3^3} b^4 \right] + \frac{2}{(-r_1 r_2)^{3/2}} \left[6 \frac{1+3a}{r_1 r_3} b d - 5 e \right], \end{aligned} \quad (\text{A2})$$

and for $f = g = 0$

$$\begin{aligned} \frac{2\pi\tau_2}{3!} &= -\frac{10}{(r_1 r_2)^4 r_4^2} \left[6 \left(1 + \frac{3}{2} a^4\right) c^3 - 2 \frac{t_{21}}{r_1 r_3^3 r_5} b^2 c^2 + \frac{t_{22}}{r_1^2 r_3^4 r_5} b^4 c - \frac{2}{3} \frac{t_{23}}{r_1^3 r_3^5 r_5} b^6 \right] \\ &+ \frac{4}{(r_1 r_2)^3 r_3^2 r_4} \left[\left\{ r_2 r_3 r_4 t_{24} d - 10 \frac{t_{25}}{r_1} b c + 10 \frac{t_{26}}{r_1^2 r_3} b^3 \right\} \frac{d}{r_5} + 5 \left\{ 2 r_3^2 (3 a^2 - 1) c - \frac{t_{27}}{r_1} b^2 \right\} e \right], \end{aligned} \quad (\text{A3})$$

where

$$\begin{aligned} t_{11} &= 6 a^4 + 12 a^3 + 6 a^2 + 4 a + 1, \\ t_{12} &= 16 a^5 + 32 a^4 + 27 a^3 + 37 a^2 + 14 a - 6, \\ t_{21} &= 54 a^9 + 234 a^8 + 339 a^7 + 222 a^6 + 164 a^5 + 54 a^4 - 152 a^3 - 94 a^2 - 6 a + 10, \\ t_{22} &= 136 a^{10} + 600 a^9 + 984 a^8 + 1144 a^7 + 1411 a^6 + 455 a^5 - 1007 a^4 - 496 a^3 + 212 a^2 + 88 a - 8, \\ t_{23} &= 56 a^{11} + 240 a^{10} + 440 a^9 + 764 a^8 + 1110 a^7 + 360 a^6 - 632 a^5 - 129 a^4 + 292 a^3 - 44 a^2 - 120 a - 24, \\ t_{24} &= 18 a^3 + 20 a^2 - 16 a - 3, \\ t_{25} &= 18 a^6 + 48 a^5 + 20 a^4 - 14 a^3 + 3 a^2 - 4 a - 2, \\ t_{26} &= 20 a^7 + 56 a^6 + 38 a^5 + 22 a^4 + 30 a^3 - 25 a^2 - 22 a + 4, \\ t_{27} &= 20 a^4 + 40 a^3 + 15 a^2 + 10 a + 4. \end{aligned}$$

2. Approximate invariant of motion

The approximate non-averaged invariant up to the fourth order in ϵ is given by:

$$\begin{aligned} \mathcal{K}^{(4)}[p, q] &= \text{C.S.} - \frac{b}{r_3} \Pi \Sigma \epsilon + \frac{b^2 - r_3 c}{r_3 r_4} \Pi^2 \epsilon^2 + C_1 \text{C.S.}^2 \epsilon^2 - \frac{\mathcal{T}_0}{r_3 r_4 r_5} \left[\Pi - \frac{\text{C.S.}}{r_3} \right] \Pi \Sigma \epsilon^3 - C_1 \frac{2b}{r_3} \Pi \Sigma \text{C.S.} \epsilon^3 \\ &+ \frac{1}{r_3^2 r_4 r_5} \left[\frac{(2 + r_2 r_4) b^4 - \mathcal{T}_1 b^2 c + r_3^2 \{ r_4 (r_3 + r_4) b d + r_5 (c^2 - r_4 e) \}}{r_3 r_6} \left(\Pi - \frac{\text{C.S.}}{r_4} \right) - 2 b \mathcal{T}_0 \frac{\text{C.S.}}{r_4} \right] \Pi^2 \epsilon^4 \\ &+ \frac{C_1}{r_3^2} \left[r_2 b^2 \Pi + \frac{(2 + 3a) b^2 - 2 r_3^2 c}{r_4} \text{C.S.} \right] \Pi^2 \epsilon^4 + C_2 \text{C.S.}^3 \epsilon^4, \end{aligned}$$

where

$$\mathcal{T}_0 = b^3 - (r_3 + r_4) b c + r_3 r_4 d \quad \text{and} \quad \mathcal{T}_1 = 3 a^3 + 7 a^2 + 6 a + 1.$$

3. Averaging procedure

Performing the averaging procedure for orders $n = 2$ and $n = 3$, where we have a single coefficient C_1 , provides:

$$C_1^{(2)} = \frac{5}{4} \frac{\mathcal{T}_0}{r_1 r_2 r_3 r_4 b},$$

$$C_1^{(3)} = \frac{T_1 b^6 - T_2 b^4 c + r_3 r_4 T_3 b^3 d + r_3 (T_4 c^2 - 7 T_5 r_3 r_4 r_5 e) b^2 - 2 r_1 r_3^2 r_4 T_6 b c d + 14 r_1 r_3^3 r_5 (r_4 e - c^2) c}{r_2 r_3 r_4 r_5 (T_7 b^4 - 4 r_1 r_3 T_8 b^2 c + 10 r_1^2 r_3^2 c^2)}.$$

At higher orders, the equations become more complex, and we encounter multiple coefficients. For clarity, we provide the results for two examples that are extensively used in our article: the generalized cubic map, $f(p) = ap + bp^2 + cp^3$:

$$C_1^{(4)} = -\frac{1}{r_3 r_4 r_5 r_6} \frac{r_4 U_1 b^6 - U_2 b^4 c + r_3 U_3 b^2 c^2 - 2 r_3^2 U_4 c^3}{U_{10} b^4 - 4 r_3 U_{11} b^2 c + 4 r_3^2 U_{12} c^2},$$

$$C_2^{(4)} = -\frac{2}{3} \frac{1}{r_1 r_2 r_3 r_4 r_5 r_6} \frac{2 r_4 (3 r_4 + 2) U_5 b^8 - U_6 b^6 c + U_7 b^4 c^2 - 2 r_3 U_8 b^2 c^3 + 4 r_3^2 U_9 c^4}{U_{10} b^4 - 4 r_3 U_{11} b^2 c + 4 r_3^2 U_{12} c^2},$$

[$d, e, f, g = 0$]

and the odd-force mapping $f_{\text{odd}}(p) = ap + cp^3 + ep^5 + gp^7 + ip^9 + \dots$, which includes, in particular, the simple cubic map $f(q) = ap + cp^3$ (remember, that for this case, the averaged coefficients must be derived from the $\overline{\mathcal{R}_n}$, rather than from \mathcal{R}_n as used in the equations above):

$$C_1^{(4-\text{odd})} = \frac{1}{r_4 (r_6 r_3)} \frac{5 V_1 c^5 - 6 r_4 V_2 c^3 e + 3 r_4^2 (r_6 r_3) V_3 c^2 g - 8 (r_2 r_1) r_4^2 V_4 c e^2 + 144 (r_2 r_1) r_4^3 (r_6 r_3) e g}{V_7 c^4 + 64 r_2 r_1 r_4 V_8 c^2 e + 56 (r_2 r_1)^2 r_4^2 e^2},$$

$$C_2^{(4-\text{odd})} = \frac{-28}{(r_2 r_1) r_4 (r_6 r_3) c} \frac{[V_5 c^2 + 4 (r_2 r_1) r_4 e] [V_6 c + r_4 (r_6 r_3) (2 c^2 - r_4 e) g]}{V_7 c^4 + 64 r_2 r_1 r_4 V_8 c^2 e + 56 (r_2 r_1)^2 r_4^2 e^2},$$

where

$$\begin{aligned} T_1 &= 13 a^3 - 47 a^2 - 80 a + 34, & V_1 &= 25 a^4 + 103 a^2 - 50, \\ T_2 &= 57 a^4 - 98 a^3 - 365 a^2 - 63 a + 93, & V_2 &= 3 a^4 + 282 a^2 - 160, \\ T_3 &= 20 a^3 - 75 a^2 - 122 a + 69, & V_3 &= 31 a^2 + 130, \\ T_4 &= 69 a^4 - 37 a^3 - 282 a^2 - 41 a + 87, & V_4 &= 43 a^2 - 28, \\ T_5 &= a - 5, & V_5 &= 3 a^2 + 10, \\ T_6 &= 19 a^2 + 21 a - 13, & V_6 &= 2 a^3 e^2 - 6 a^2 c^2 e + 3 a c^4 + c^2 e, \\ T_7 &= 5 a^2 - 34 a + 69, & V_7 &= 29 a^4 + 140 a^2 + 500, \\ T_8 &= 3 a - 13, & V_8 &= a^2 + 5, \end{aligned}$$

and

$$\begin{aligned} U_1 &= (a^3 + 2 a^2 + 2 a + 2)(15 a^3 + 30 a^2 + 8 a - 18), \\ U_2 &= 72 a^8 + 299 a^7 + 549 a^6 + 634 a^5 + 380 a^4 - 131 a^3 - 288 a^2 - 60 a + 18, \\ U_3 &= 82 a^8 + 324 a^7 + 655 a^6 + 764 a^5 + 168 a^4 - 507 a^3 - 344 a^2 + 8 a + 36, \\ U_4 &= 12 a^8 + 58 a^7 + 143 a^6 + 122 a^5 - 78 a^4 - 162 a^3 - 56 a^2 + 16 a + 9, \\ U_5 &= 15 a^3 + 22 a^2 + 12 a + 20, \\ U_6 &= 468 a^6 + 1278 a^5 + 1518 a^4 + 1557 a^3 + 962 a^2 + 108 a - 20, \\ U_7 &= 809 a^7 + 2838 a^6 + 4620 a^5 + 5131 a^4 + 3423 a^3 + 652 a^2 - 356 a - 80, \\ U_8 &= 291 a^7 + 987 a^6 + 1697 a^5 + 1738 a^4 + 616 a^3 - 407 a^2 - 342 a - 50, \\ U_9 &= (4 a^3 + 11 a^2 + 20 a + 10)(9 a^4 + 8 a^3 - 5 a^2 - 6 a - 1), \\ U_{10} &= 11 a^6 + 32 a^5 + 40 a^4 + 60 a^3 + 80 a^2 + 64 a + 36, \\ U_{11} &= 3 a^6 + 12 a^5 + 26 a^4 + 41 a^3 + 56 a^2 + 52 a + 18, \\ U_{12} &= a^6 + 4 a^5 + 10 a^4 + 26 a^3 + 48 a^2 + 36 a + 9. \end{aligned}$$

Additionally, upon request, we can provide a **Wolfram Mathematica** file with simplified expressions for the general force mapping up to ϵ^6 , as well as for the mixed force (generalized cubic) $f_{MX}(p) = ap + bp^2 + cp^3$ up to ϵ^8 , the quadratic map up to ϵ^{10} , and the simple cubic map ($b = 0$) up to ϵ^{16} .

4. Normal form of approximate invariant for low order resonances

Consider a general map in McMillan form with a force function

$$f(q) = aq + bq^2 + cq^3 + dq^4 + eq^5 + fq^6 + \dots$$

Below, we present the converged lower-order terms of the averaged invariant $\langle \mathcal{K} \rangle [p, q]$ at selected primary resonances. For the third-integer resonance $\nu_0 = 1/3$ (i.e., $a = -1$), we obtain:

$$\begin{aligned} b \neq 0: & -b \Pi \Sigma \epsilon - \left[b^2 \Pi^2 - (b^2 + c) \frac{\text{C.S.}^2}{2} \right] \epsilon^2 - b \left[(b^2 + c) \Pi - \left(b^2 - c - 2 \frac{d}{b} \right) \frac{\text{C.S.}}{2} \right] \Pi \Sigma \epsilon^3 + \mathcal{O}(\epsilon^4), \\ b = 0: & c \frac{\text{C.S.}^2}{2} \epsilon^2 - d \Pi \Sigma \text{C.S.} \epsilon^3 + \frac{1}{2} \left[(c^2 + e) \Pi^3 + (3c^2 + e) \Pi^2 \text{C.S.} - \frac{3c^2 - 2e}{3} \text{C.S.}^3 \right] \epsilon^4 \\ & - \left[cd \Pi^2 - (cd - 2f) \frac{\text{C.S.}^2}{2} \right] \Pi \Sigma \epsilon^5 + \mathcal{O}(\epsilon^6). \end{aligned}$$

For the fourth-integer resonance $\nu_0 = 1/4$ (i.e., $a = 0$), we find:

$$\begin{aligned} b \neq 0: & \left[(b^2 - c) \Pi^2 + c \frac{\text{C.S.}^2}{2} \right] \epsilon^2 + b \left[(b^2 - c) \Pi - b^2 \text{C.S.} \right] \Pi \Sigma \epsilon^3 \\ & + \left[(2b^4 - c^2) \Pi^3 - \left(b^4 - \frac{3}{2} b^2 c - bd + e \right) \Pi^2 \text{C.S.} + (b^4 + e) \frac{\text{C.S.}^3}{3} \right] \epsilon^4 \\ & + b \left[\left(b^4 - c^2 - c \frac{d}{b} + e \right) \Pi^2 - (b^4 - b^2 c + c^2 - 2bd + e) \Pi \text{C.S.} - (b^2 c - c^2 + 2bd) \text{C.S.}^2 \right] \Pi \Sigma \epsilon^5 \\ & + \mathcal{O}(\epsilon^6), \\ b = 0: & -c \left[\Pi^2 - \frac{\text{C.S.}^2}{2} \right] \epsilon^2 - \left[c^2 \Pi^3 + e \Pi^2 \text{C.S.} - e \frac{\text{C.S.}^3}{3} \right] \epsilon^4 - cd \Pi^3 \Sigma \epsilon^5 + \mathcal{O}(\epsilon^6). \end{aligned}$$

For the resonance $\nu_0 = 1/6$ (i.e., $a = 1$), the result is:

$$\begin{aligned} b \neq 0: & (b^2 + c) \frac{\text{C.S.}^2}{2} \epsilon^2 - b(b^2 + c) \frac{\Pi \Sigma \text{C.S.}}{2} \epsilon^3 + \mathcal{O}(\epsilon^4), \\ b, c = 0: & -\frac{e}{2} \left[\Pi^3 - \left(\Pi^2 + \frac{2}{3} \text{C.S.}^2 \right) \text{C.S.} \right] \epsilon^4 + \mathcal{O}(\epsilon^6). \end{aligned}$$

For the fifth-order resonances $\nu_0 = 1/5$ and $\nu_0 = 2/5$ we obtain the corresponding averaged invariant

$$\begin{aligned} d, e = 0: & a_r \frac{2b^2 + 3c}{2} \text{C.S.}^2 \epsilon^2 - b \left[\{b^2 - (2a_r + 1)c\} \Pi - \{(3a_r - 2)b^2 + (4a_r - 5)c\} \text{C.S.} \right] \Pi \Sigma \epsilon^3 + \mathcal{O}(\epsilon^4), \\ b, c = 0: & -d(\Pi - a_r \text{C.S.}) \Pi \Sigma \epsilon^3 + 2e \frac{3a_r - 1}{3} \text{C.S.}^3 \epsilon^4 + f \left[(a_r - 2) \Pi + (3a_r - 1) \text{C.S.} \right] \Pi \Sigma \text{C.S.} \epsilon^5 + \mathcal{O}(\epsilon^6), \end{aligned}$$

with the corresponding values of the trace parameter are

$$a_r = a_{1/5, 2/5} = \frac{-1 \pm \sqrt{5}}{2}.$$

For the quadratic Hénon map, where $f(q) = a q + b q^2$, one obtains:

$$\begin{aligned}
r_4 : & \quad b^2 \Pi^2 \epsilon^2 + b^3 (\Pi - \text{C.S.}) \Pi \Sigma \epsilon^3 + b^4 \left(2 \Pi^3 - \Pi^2 \text{C.S.} + \frac{\text{C.S.}^3}{3} \right) \epsilon^4 + b^5 (\Pi - \text{C.S.}) \Pi^2 \Sigma \epsilon^5 + \mathcal{O}(\epsilon^6), \\
r_3 : & \quad -b \Pi \Sigma \epsilon - b^2 \left[\Pi^2 - \frac{\text{C.S.}^2}{2} \right] \epsilon^2 - b^3 \left[\Pi - \frac{\text{C.S.}}{2} \right] \Pi \Sigma \epsilon^3 + \mathcal{O}(\epsilon^4), \\
r_6 : & \quad \frac{b^2}{2} \text{C.S.}^2 \epsilon^2 - \frac{b^3}{2} \Pi \Sigma \text{C.S.} \epsilon^3 + b^4 \left[\Pi^3 + \frac{2}{3} \text{C.S.}^3 \right] \epsilon^4 + b^5 \left[\Pi^2 - 3 \Pi \text{C.S.} + \frac{1}{2} \text{C.S.}^2 \right] \Pi \Sigma \epsilon^5 + \mathcal{O}(\epsilon^6), \\
r_5 : & \quad b^2 a_r \text{C.S.}^2 \epsilon^2 - b^3 [\Pi - (3 a_r - 2) \text{C.S.}] \Pi \Sigma \epsilon^3 - b^4 \left[3 \Pi^3 - (7 a_r + 1) \Pi^2 \text{C.S.} + \frac{2}{3} (2 a_r - 1) \text{C.S.}^3 \right] \epsilon^4, \\
& \quad + b^5 [2 (a_r - 3) \Pi^2 + 3 (2 a_r + 1) \Pi \text{C.S.} - (3 a_r + 2) \text{C.S.}^2] \Pi \Sigma \epsilon^5 + \mathcal{O}(\epsilon^6), \quad a_r = a_{1/5,2/5} = \frac{-1 \pm \sqrt{5}}{2}, \\
r_8 : & \quad b^2 (2 a_r + 1) \text{C.S.}^2 \epsilon^2 + 2 b^3 (a_r - 3) \Pi \Sigma \text{C.S.} \epsilon^3 + \mathcal{O}(\epsilon^4), \quad a_r = a_{1/8,3/8} = \pm \sqrt{2}, \\
r_{10} : & \quad b^2 (3 a_r + 2) \text{C.S.}^2 \epsilon^2 - 2 b^3 (a_r + 1) \Pi \Sigma \text{C.S.} \epsilon^3 + \mathcal{O}(\epsilon^4), \quad a_r = a_{1/10,3/10} = \frac{1 \pm \sqrt{5}}{2}.
\end{aligned}$$

For the simple cubic Hénon map, where $f(q) = a q + c q^3$, the expressions become

$$\begin{aligned}
r_4 : & \quad -c \left[\Pi^2 - \frac{\text{C.S.}^2}{2} \right] \epsilon^2 - c^2 \Pi^3 \epsilon^4 + \mathcal{O}(\epsilon^6), \quad r_{3,6} : \quad \frac{c}{2} \text{C.S.}^2 \epsilon^2 + \frac{c^2}{2} [\Pi^3 - a_r (3 \Pi^2 - \text{C.S.}^2) \text{C.S.}] \epsilon^4 + \mathcal{O}(\epsilon^6), \\
r_{5,10} : & \quad \frac{3}{2} c a_r \text{C.S.}^2 \epsilon^2 + \mathcal{O}(\epsilon^4), \quad r_8 : \quad \frac{3}{2} c a_r \text{C.S.}^2 \epsilon^2 - c^2 (3 \Pi^2 - 5 \text{C.S.}^2) \text{C.S.} \epsilon^4 + \mathcal{O}(\epsilon^6).
\end{aligned}$$

-
- [1] Andrey Nikolaevich Kolmogorov, “On conservation of conditionally periodic motions for a small change in Hamilton’s function,” (1954) pp. 527–530.
- [2] Jürgen Moser, “On invariant curves of area-preserving mapping of an annulus,” *Matematika* **6**, 51–68 (1962).
- [3] Vladimir I. Arnold, “Proof of a theorem of A. N. Kolmogorov on the preservation of conditionally periodic motions under a small perturbation of the Hamiltonian,” *Russian Mathematical Surveys* **18**, 9–36 (1963).
- [4] N. N. Nekhoroshev, “Behavior of Hamiltonian systems close to integrable,” *Functional Analysis and Its Applications* **5**, 338–339 (1971).
- [5] Karl Friedrich Siburg, “1. aubry-mather theory,” in *The Principle of Least Action in Geometry and Dynamics* (Springer Berlin Heidelberg, Berlin, Heidelberg, 2004) pp. 1–13.
- [6] V. I. Arnold, “Instability of dynamical systems with several degrees of freedom,” in *Collected Works: Representations of Functions, Celestial Mechanics and KAM Theory, 1957–1965*, edited by Alexander B. Givental, Boris A. Khesin, Jerrold E. Marsden, Alexander N. Varchenko, Victor A. Vassiliev, Oleg Ya. Viro, and Vladimir M. Zakalyukin (Springer Berlin Heidelberg, Berlin, Heidelberg, 2009) pp. 423–427.
- [7] E. Noether, “Invariante Variationsprobleme,” *Nachrichten von der Gesellschaft der Wissenschaften zu Göttingen, Mathematisch-Physikalische Klasse* **1918**, 235–257 (1918).
- [8] Rubens M Marinho, “Noether’s theorem in classical mechanics revisited,” *European Journal of Physics* **28**, 37 (2006).
- [9] Michael E. Peskin and Daniel V. Schroeder, *An Introduction to quantum field theory* (Addison-Wesley, Reading, USA, 1995) pp. 17, 60, 308–310, 683.
- [10] Carl Ludwig Siegel and Jürgen K. Moser, *Lectures on Celestial Mechanics*, 1st ed., *Classics in Mathematics* (Springer Berlin, Heidelberg, 1971).
- [11] Vladimir I. Arnold, Valery V. Kozlov, and Anatoly I. Neishtadt, *Mathematical Aspects of Classical and Celestial Mechanics*, 3rd ed., *Encyclopaedia of Mathematical Sciences* (Springer Berlin, Heidelberg, 2006).
- [12] Federico Mogavero, Nam H. Hoang, and Jacques Laskar, “Timescales of chaos in the inner solar system: Lyapunov spectrum and quasi-integrals of motion,” *Phys. Rev. X* **13**, 021018 (2023).
- [13] M. Giovannozzi, W. Scandale, and E. Todesco, “Dynamic aperture extrapolation in the presence of tune modulation,” *Phys. Rev. E* **57**, 3432–3443 (1998).
- [14] A. Bazzani, M. Giovannozzi, E. H. Maclean, C. E. Montanari, F. F. Van der Veken, and W. Van Goethem, “Advances on the modeling of the time evolution of dynamic aperture of hadron circular accelerators,” *Phys. Rev. Accel. Beams* **22**, 104003 (2019).
- [15] George D. Birkhoff, “Dynamical systems with two degrees of freedom,” *Transactions of the American Mathematical Society* **18**, 199–300 (1917).

- [16] René DeVogelaere, “IV. On the structure of symmetric periodic solutions of conservative systems, with applications,” in *Contributions to the Theory of Nonlinear Oscillations (AM-41), Volume IV*, edited by Solomon Lefschetz (Princeton University Press, 1958) pp. 53–84.
- [17] Daniel C. Lewis Jr., “Reversible transformations,” *Pacific Journal of Mathematics* **11**, 1077–1087 (1961).
- [18] J.A.G. Roberts and G.R.W. Quispel, “Chaos and time-reversal symmetry. order and chaos in reversible dynamical systems,” *Physics Reports* **216**, 63–177 (1992).
- [19] Tim Zolkin, Sergei Nagaitsev, Ivan Morozov, Sergei Kladov, and Young-Kee Kim, “Isochronous and period-doubling diagrams for symplectic maps of the plane,” (2024), arXiv:2412.05541 [nlin.CD].
- [20] Ernest D. Courant and Hartland S. Snyder, “Theory of the alternating-gradient synchrotron,” *Annals of Physics* **3**, 1–48 (1958).
- [21] Michelotti Leo, *Intermediate classical dynamics with applications to beam physics* (Wiley, New York, 1995) pp. 284–299.
- [22] Berz Martin, “Chapter 7 - repetitive systems,” in *Modern Map Methods in Particle Beam Physics*, Advances in Imaging and Electron Physics, Vol. 108, edited by Peter Hawkes (Elsevier, 1999) pp. 270–288.
- [23] Étienne Forest, *Beam Dynamics: A New Attitude and Framework*, The Physics and Technology of Particle and Photon Beams, Vol. 8 (Hardwood Academic / CRC Press, Amsterdam, The Netherlands, 1998) pp. 138–141.
- [24] Ivan Morozov and Evgeny Levichev, “Dynamical aperture control in accelerator lattices with multipole potentials,” in *Proceedings of the CERN-BINP Workshop for Young Scientists in e^+e^- Colliders, Geneva, Switzerland, 22 – 25 August 2016*, CERN Proceedings, Vol. 1/2017, edited by Valeria Brancolini and Lucie Linssen (CERN, Geneva, 2017) pp. 195–206, CERN-Proceedings-2017-001.
- [25] Johan Bengtsson, *The sextupole scheme for the Swiss Light Source (SLS): an analytic approach*, Tech. Rep. SLS-TME-TA-1997-0009 (Paul Scherrer Institut, Villigen, Switzerland, 1997).
- [26] Bingfeng Wei, Zhenghe Bai, Jiajie Tan, Lin Wang, and Guangyao Feng, “Minimizing the fluctuation of resonance driving terms in dynamic aperture optimization,” *Phys. Rev. Accel. Beams* **26**, 084001 (2023).
- [27] Bingfeng Wei, Zhenghe Bai, Guangyao Feng, Alexandre Loulergue, Laurent S. Nadolski, and Ryutaro Nagaoka, “Analysis of off-momentum nonlinear driving terms for enlarging off-momentum dynamic apertures,” *Phys. Rev. Accel. Beams* **27**, 104001 (2024).
- [28] Lev Landau, “61 - on the vibrations of the electronic plasma,” in *Collected Papers of L.D. Landau*, edited by D. TER HAAR (Pergamon, 1965) pp. 445–460.
- [29] J. H. Malmberg and C. B. Wharton, “Collisionless damping of electrostatic plasma waves,” *Phys. Rev. Lett.* **13**, 184–186 (1964).
- [30] Jacques Gareyte, Jean-Pierre Koutchouk, and F Ruggiero, *Landau damping dynamic aperture and octupole in LHC*, Tech. Rep. (CERN, Geneva, 1997) revised version number 1 submitted on 2003-08-21 14:12:02.
- [31] V. Shiltsev, Y. Alexahin, A. Burov, and A. Valishev, “Landau damping of beam instabilities by electron lenses,” *Phys. Rev. Lett.* **119**, 134802 (2017).
- [32] Allan J Lichtenberg and Michael A Lieberman, *Regular and chaotic dynamics*, 2nd ed., Applied Mathematical Sciences (AMS), Vol. 38 (Springer New York, NY, 2003).
- [33] Georg Duffing, *Erzwungene Schwingungen bei veränderlicher Eigenfrequenz und ihre technische Bedeutung. (German). Forced oscillations with changing natural frequencies and their technical significance* (Vieweg & Sohn, 1918).
- [34] V.I. Arnold and A. Avez, *Ergodic Problems of Classical Mechanics*, Advanced book classics (Addison-Wesley, 1989).
- [35] Boris V. Chirikov, “Research concerning the theory of non-linear resonance and stochasticity,” (1971), translated at CERN by A. T. Sanders from the Russian [CERN-Trans-71-40]. Nuclear Physics Institute of the Siberian Section of the USSR Academy of Science, Report 267, Novosibirsk, 1969 [IYAF-267-TRANS-E].
- [36] Boris V. Chirikov, “A universal instability of many-dimensional oscillator systems,” *Physics Reports* **52**, 263–379 (1979).
- [37] Michel Hénon and Carl Heiles, “The applicability of the third integral of motion: some numerical experiments,” *The Astronomical Journal* **69**, 73–79 (1964).
- [38] Edwin M. McMillan, “A problem in the stability of periodic systems,” in *Topics in modern physics. A Tribute to Edward U. Condon*, edited by W. E. Brittin and H. Odabasi (Colorado Associated University Press, Boulder, CO, 1971) pp. 219–244.
- [39] Yuri B. Suris, “Integrable mappings of the standard type,” *Functional Analysis and Its Applications* **23**, 74–76 (1989).
- [40] Morton Brown, “A periodic homeomorphism of the plane,” in *Continuum theory and dynamical systems*, Lecture Notes in Pure and Appl. Math. No. 149 (Marcel Dekker AG, New York, 1993) pp. 83–87.
- [41] T. Zolkin, Y. Kharkov, and S. Nagaitsev, “Machine-assisted discovery of integrable symplectic mappings,” *Phys. Rev. Res.* **5**, 043241 (2023).
- [42] T. Zolkin, Y. Kharkov, and S. Nagaitsev, “Integrable symplectic maps with a polygon tessellation,” *Phys. Rev. Res.* **6**, 023324 (2024).
- [43] Michel Hénon, “Numerical study of quadratic area-preserving mappings,” *Quarterly of Applied Mathematics* **27**, 291–312 (1969).
- [44] D. Sterling, H.R. Dullin, and J.D. Meiss, “Homoclinic bifurcations for the Hénon map,” *Physica D: Nonlinear Phenomena* **134**, 153–184 (1999).
- [45] H.R. Dullin, J.D. Meiss, and D. Sterling, “Generic twistless bifurcations,” *Nonlinearity* **13**, 203 (2000).
- [46] H.R. Dullin and J.D. Meiss, “Generalized Hénon maps: the cubic diffeomorphisms of the plane,” *Physica D: Nonlinear Phenomena* **143**, 262–289 (2000).
- [47] V. I. Arnold, “Small denominators. I. Mapping of the circumference onto itself,” in *Collected Works: Representations of Functions, Celestial Mechanics and KAM Theory, 1957–1965*, edited by Alexander B. Givental, Boris A. Khesin, Jerrold E.

- Marsden, Alexander N. Varchenko, Victor A. Vassiliev, Oleg Ya. Viro, and Vladimir M. Zakalyukin (Springer, Berlin, Heidelberg, 2009) pp. 152–223.
- [48] Philip L. Boyland, “Bifurcations of circle maps: Arnol’d tongues, bistability and rotation intervals,” *Communications in Mathematical Physics* **106**, 353 – 381 (1986).
- [49] Nikolai Yu. Ivankov and Sergey P. Kuznetsov, “Complex periodic orbits, renormalization, and scaling for quasiperiodic golden-mean transition to chaos,” *Phys. Rev. E* **63**, 046210 (2001).
- [50] Tim Zolkin, Sergei Nagaitsev, and Ivan Morozov, “Dynamics of McMillan mappings I. McMillan multipoles,” (2024), arXiv:2405.05652 [nlin.SI].
- [51] Tim Zolkin, Sergei Nagaitsev, Ivan Morozov, Sergei Kladov, and Young-Kee Kim, “Dynamics of McMillan mappings III. Symmetric map with mixed nonlinearity,” (2024), arXiv:2410.10380 [nlin.SI].
- [52] Apostolos Iatrou and John A. G. Roberts, “Integrable mappings of the plane preserving biquadratic invariant curves,” *Journal of Physics A: Mathematical and General* **34**, 6617 (2001).
- [53] Apostolos Iatrou and John A. G. Roberts, “Integrable mappings of the plane preserving biquadratic invariant curves II,” *Nonlinearity* **15**, 459–489 (2002).
- [54] Apostolos Iatrou and John A. G. Roberts, “Integrable mappings of the plane preserving biquadratic invariant curves III,” *Physica A: Statistical Mechanics and its Applications* **326**, 400–411 (2003).
- [55] Li Hua Yu, “Analysis of nonlinear dynamics by square matrix method,” *Phys. Rev. Accel. Beams* **20**, 034001 (2017).
- [56] Li Hua Yu, Yoshiteru Hidaka, Victor Smaluk, Kelly Anderson, and Yue Hao, “Convergence map with action-angle variables based on square matrix for nonlinear lattice optimization,” *Phys. Rev. Accel. Beams* **26**, 054002 (2023).
- [57] I. Morozov, “square,” <https://github.com/i-a-morozov/square> (2024).
- [58] Timofey Zolkin, Sergei Nagaitsev, and Viatcheslav Danilov, “Rotation number of integrable symplectic mappings of the plane,” (2017), arXiv:1704.03077 [nlin.SI].
- [59] Sergei Nagaitsev and Timofey Zolkin, “Betatron frequency and the Poincaré rotation number,” *Phys. Rev. Accel. Beams* **23**, 054001 (2020).
- [60] Chad E. Mitchell, Robert D. Ryne, Kilean Hwang, Sergei Nagaitsev, and Timofey Zolkin, “Extracting dynamical frequencies from invariants of motion in finite-dimensional nonlinear integrable systems,” *Phys. Rev. E* **103**, 062216 (2021).
- [61] Tim Zolkin, Brandon Cathey, and Sergei Nagaitsev, “Dynamics of McMillan mappings II. Axially symmetric map,” (2024), arXiv:2405.05657 [nlin.SI].
- [62] Li Hua Yu, “Analysis of nonlinear dynamics by square matrix method,” *Phys. Rev. Accel. Beams* **20**, 034001 (2017).
- [63] Leo P. Michelotti, *Intermediate Classical Dynamics with Applications to Beam Physics*, Wiley Series in Beam Physics and Accelerator Technology (Wiley, 1995).
- [64] F. Panichi, L. Ciotti, and G. Turchetti, “Fidelity and reversibility in the restricted three body problem,” *Communications in Nonlinear Science and Numerical Simulation* **35**, 53–68 (2016).
- [65] Federico Panichi, Krzysztof Goździewski, and Giorgio Turchetti, “The reversibility error method (REM): a new, dynamical fast indicator for planetary dynamics,” *Monthly Notices of the Royal Astronomical Society* **468**, 469–491 (2017), <https://academic.oup.com/mnras/article-pdf/468/1/469/11066230/stx374.pdf>.
- [66] A. Bazzani, M. Giovannozzi, C. E. Montanari, and G. Turchetti, “Performance analysis of indicators of chaos for nonlinear dynamical systems,” *Phys. Rev. E* **107**, 064209 (2023).
- [67] Gilles Reinout Willem Quispel, Jhon A. G. Roberts, and Colin J. Thompson, “Integrable mappings and soliton equations,” *Physics Letters A* **126**, 419–421 (1988).
- [68] Gilles Reinout Willem Quispel, Jhon A. G. Roberts, and Colin J. Thompson, “Integrable mappings and soliton equations II,” *Physica D: Nonlinear Phenomena* **34**, 183–192 (1989).